Pergamon

Int. J. Heat Mass Transfer. Vol. 37, No. 16, pp. 2475–2504, 1994

0017–9310/94 $7.00 + 0.00

0017–9310(94)E0062–Y

An investigation and comparative analysis of two- and three-dimensional turbulent natural convection in a horizontal annulus

C. P. DESAI and K. VAFAI†

Mechanical Engineering Department, The Ohio State University, Columbus, OH 43210, U.S.A.

(*Received* 8 *November* 1993 *and in final form* 24 *February* 1994)

Abstract—In the present study, simulation of turbulent buoyancy-driven flow in an annulus bounded by concentric, horizontal cylinders and adiabatic end walls has been carried out. Time-averaged equations of turbulent fluid motion and heat transfer were solved using a wall function approach coupled with the standard k–ε model. Discretization of the governing equations was achieved using a finite element scheme based on the Galerkin method of weighted residuals. Using a two-dimensional analysis, results were obtained for Rayleigh numbers ranging from 10^6 to 10^9 and the effects of Prandtl number and radius ratio on the flow and heat transfer characteristics were thoroughly examined. A wide range of parameters ($10^6 < Ra < 10^9$, $0.01 < Pr < 5000$, $1.5 < R < 11$) was considered in the present study. A comprehensive comparative analysis establishing a unified treatment of previous experimental and computational results is presented. A good agreement was found between the results from this investigation and previous works. Results obtained from a three-dimensional model are also presented to describe more realistic three-dimensional flow characteristics. It is shown that, if the annulus is sufficiently long, there exists a core region over a substantial length of the cavity, which can be approximated by a two-dimensional model.

INTRODUCTION

NATURAL convection in annular cavities bounded by co-axial, horizontal cylinders has been investigated widely in the past owing to the number of practical applications associated with this geometry such as heat transfer and fluid flow in nuclear reactors, thermal storage systems, electrical transmission cables, and electronic component cooling among others. A detailed literature review of early research pertinent to this geometry can be found in Kuehn and Goldstein [1]. In their work, a thorough two-dimensional investigation was carried out covering the range of Rayleigh numbers from pure conduction to the laminar boundary layer regime. Transient results for this geometry were presented by Tsui and Tremblay [2]. Results for two-dimensional, laminar, buoyancy-induced flows have been established to an extent that this configuration is used as a source of comparison for validating relevant numerical codes. The effect of a constant heat flux on the inner cylinder as compared to an isothermal inner cylinder has also been studied (Kumar [3] and Castrejon and Spalding [4]).

It is known that, due to the viscous shearing effects at the end walls, a three-dimensional analysis of buoyancy-induced flow and heat transfer is necessary when the annulus has a finite length. Takata *et al.* [5] performed an analytical and experimental investigation of natural convection in an inclined cylindrical annulus with a heated inner and cooled outer cylinder. Their results revealed the existence of a co-axial double helical flow pattern inside the cavity. However, their results were obtained only for a high Prandtl number fluid ($Pr = 5000$) and therefore limited their range of practical applicability. A three-dimensional analysis for air ($Pr = 0.7$) was presented by Fusegi and Farouk [6] for a differentially heated annulus. The small cylinder length considered by them ensured that the end-wall effects were evident in the fluid motion. In a recent study, Vafai and Ettefagh [7] carried out a numerical study of the transient, three-dimensional natural convection process in a horizontal annulus. A detailed explanation of the development of the flow and temperature fields is presented in their work. To accurately detect the two-dimensional nature of the flow field in the core region, an annulus with a length-to-outer radius ratio of at least 4 was used. Their results show that for the aspect ratio considered, the temperature distribution within the core region of the annulus remains unchanged.

Experimental studies (Kuehn and Goldstein [1]) using air as a working fluid suggested the transition from laminar to turbulent flow when the Rayleigh number (based on gap width) approaches 10^6 for a radius ratio of 2.6. The transition Rayleigh number

† Author to whom all correspondence should be addressed.

NOMENCLATURE

k	turbulent kinetic energy
L	gap width, $R_o - R_i$
L_a	length of the annular enclosure
n	outward normal from the surface
Pr	Prandtl number, ν/α
Pr_t	turbulent Prandtl number
p	pressure
R	radius ratio, R_o/R_i
Ra	Rayleigh number, $g\beta\Delta TL^3/\nu\alpha$
R_i	radius of the inner cylinder
R_o	radius of the outer cylinder
T	temperature
T^+	temperature obtained from the universal near-wall profile
T_i	temperature of the inner cylinder
T_o	temperature of the outer cylinder
U	characteristic velocity, $(\alpha/L)\sqrt{Ra\,Pr}$
u^+	velocity obtained from the universal near-wall profile.

Greek symbols

α	thermal diffusivity
β	volume expansion coefficient
Δ	height of the wall element
ε	dissipation of turbulent K.E.
ε_p	turbulent dissipation at the first grid point away from the wall.
κ	Von Karman constant
λ	thermal conductivity
λ_t	turbulent thermal conductivity
λ_{eff}	effective thermal conductivity
μ	dynamic viscosity
μ_t	turbulent viscosity
μ_{eff}	effective viscosity
ν	kinematic viscosity

Subscripts

l	laminar
t	turbulent.

depends on the radius ratio of the annular geometry and the Prandtl number of the working fluid. Theoretical studies to simulate turbulent processes are extremely difficult owing to the fact that resolution of the small-scale eddies (to capture the details of the flow) poses a massive computational task. The complete simulation of a turbulent flow problem could involve the solution of the unsteady Navier–Stokes equations (direct numerical simulation—DNS). However, the mesh size and the time-step size required to capture the details of the flow field must be very small thus necessitating the need for large amounts of computer memory and CPU time. Modeling approaches therefore rely on solutions for the time-averaged values of the turbulent quantities.

While the study of forced convection turbulent flows has advanced to some extent, theoretical research involving simulation of turbulent natural convection processes is still in a premature stage. A major portion of the research pertinent to turbulent buoyancy-induced flows is limited to flow near hot, vertical walls. A comprehensive literature review of the studies carried out for flow near a vertical, heated wall is mentioned elsewhere [8]. To date, reported results on turbulent natural convection in cavity type configurations have been very limited. Markatos *et al.* [9] developed a computational procedure for calculating natural convection flows in enclosures containing a fire source. The k–ε model of Launder and Spalding [10] was used to obtain results in their study which was motivated by the need to investigate buoyancy-induced smoke flow in enclosures. In another study, Markatos and Pericleous [11] studied turbulent natural convection in a square cavity with differentially heated side walls. Results were presented for air up to Rayleigh numbers of 10^{16}. Their study also included a thorough grid-independence study including the use of a very fine mesh in near wall regions for higher Rayleigh numbers. Ozoe *et al.* [12] also utilized the k–ε turbulence model to compute turbulent natural convection of water in rectangular channels. The Nusselt number and flow field results obtained by them agreed well with available experimental and numerical data. It appeared that a more refined turbulence model and finer grid divisions were required, particularly for high Rayleigh numbers. Their study included sensitivity tests to examine the effects of changing some of the constants of the k–ε model. Humphrey and To [13] predicted steady free and mixed convection in open rectangular cavities of several rectangular cross-sections and orientations by extending the low Reynolds number approximation proposed by Jones and Launder [14]. Essentially, this involved calculations all the way down to the viscous sublayer. Damping of turbulent fluctuations in the near-wall region were simulated by using a Van Driest relation for variation of turbulent viscosity. Henkes *et al.* [15] studied natural convection in a square cavity with three different turbulent models: (i) the standard k–ε approach with wall functions; (ii) the low Reynolds number model of Chien [16]; and (iii) the low Reynolds number model of Jones and Launder [14]. Comparisons against experimental data showed that the low Reynolds number models gave better predictions than the standard k–ε model with wall functions.

Relatively little amount of experimental work has been done to study buoyancy-induced annular flow in the turbulent regime. Kuehn and Goldstein [17] have presented some experimental data for natural convection in concentric and eccentric annuli. Most of

their data, however, lie in the laminar regime though some results have been presented in the turbulent regime ($Ra > 10^6$). More recently, an experimental study of turbulent natural convection of helium in a horizontal annulus at cryogenic temperatures was performed by Bishop [18]. He presented results showing time-averaged temperature profiles and overall heat transfer rates for gap-width Rayleigh numbers ranging from 6×10^6 to 2×10^9. The expansion number ($\beta\Delta T$) ranged from 0.25 to 1.0 for a constant $Pr = 0.688$ and diameter ratio of 3.36. They concluded that the heat transfer results are significantly affected by the value of the expansion number as well as the Rayleigh number. McLeod and Bishop [19] used the same experimental set-up of Bishop [18] for a radius ratio of 4.85 and gap-width Rayleigh numbers ranging from 8×10^6 to 2×10^9. The nature and extent of the turbulence in the convective flow was presented by means of the fluctuations in temperature. Their study further verified the conclusions derived by Bishop [18] that a higher expansion number implies a lower core temperature, resulting in higher heat transfer rates.

To the best of the authors' knowledge, the works of Farouk and Guceri [20], Fukuda *et al.* [21, 22] and Morita *et al.* [23] are the only reported theoretical results pertinent to turbulent natural convection in an annular geometry. Using a two-dimensional approach, Farouk and Guceri [20] obtained numerical solutions of the steady-state, buoyancy-induced flow in an annulus. They used a k–ε turbulence model proposed by Launder and Spalding [10] for forced convection flows. Turbulent flow results were presented for Rayleigh numbers of 10^6 and 10^7. A radius ratio of 2.6 was used to obtain the results, which were also compared with some of the experimental data presented by Kuehn and Goldstein [1]. Fukuda *et al.* [21] carried out a direct numerical simulation (DNS) of turbulent natural convection in a horizontal annulus using an explicit leap-frog scheme. A radius ratio of 2 was used. Both oscillatory and turbulent flow were realized for Rayleigh numbers up to 6×10^5. They found that DNS simulated the flow pattern and isotherms fairly well. All results were verified by measurements of the velocity and temperature fields and their turbulent characteristics measured with a hot wire anemometer and thermocouples, respectively. Fukuda *et al.* [22] obtained three-dimensional results for Rayleigh numbers up to 1.18×10^9, using DNS and large eddy simulation (LES). Comparison with experimental data showed good agreement. Morita *et al.* [23] also simulated three-dimensional, unsteady turbulent natural convection in an annulus to demonstrate the validity of DNS for this category of problems.

Both two-dimensional and three-dimensional simulations related to turbulent natural convection in annular cavities are very rare. There is a need to model high Rayleigh number natural convection processes because a significant number of real-life problems involving natural convection are indeed in the turbulent regime. In the present study, simulations of turbulent natural convection in a horizontal annulus have been investigated. Results were obtained using both a two-dimensional (infinitely long annulus) and a three-dimensional model (annulus with finite length). The standard k–ε turbulence model combined with specialized wall elements to account for the low Reynolds number effects in the near-wall region was used. Results presented here have been obtained using a program based on the Galerkin method of weighted residuals [29]. A wide range of Rayleigh numbers has been considered in the present study. Furthermore, the role played by the radius ratio and the thermophysical properties of the working fluid in enhancing or decreasing heat transfer rates in the annulus have been considered. These are important aspects from an engineering design point of view. Detailed grid-independence and parametric studies were implemented using the two-dimensional model. The three-dimensional analyses reveals some of the important features of the flow and temperature fields similar to those in the laminar regime.

This study thus provides useful data on turbulent natural convection in an annular geometry. The wide range of Rayleigh numbers, thermophysical properties and annulus dimensions examined make the presented information in this work very useful from an application point of view. To the best of the authors' knowledge, these are the first documented results on three-dimensional turbulent natural convection along with information on axial effects. Even though three-dimensional simulations (Fukuda *et al.* [21, 22], Morita *et al.* [23]) of this problem have been carried out in the past, the influence of the axial end-walls on the flow and temperature fields has not been studied at all. Virtually nothing has been mentioned to explain the three-dimensional characteristics of the various flow variables in the turbulent regime. The three-dimensional results documented in the present work attempts to enhance the understanding of this aspect of the problem. It is also shown that, for a sufficiently long annulus, the variable field in the core region of the cavity can be calculated accurately by a two-dimensional analysis. An additional contribution of this work is the detailed investigation of various thermophysical and geometric characteristics of the two-dimensional turbulent natural convection which has not been done before. Therefore, these results should serve as a stepping stone toward the study of more complicated turbulent buoyancy-induced processes in the future.

ANALYSIS

Governing equations

The physical model used in the present study (shown in Fig. 1) comprises of an annular gap enclosed between two concentric, horizontal cylinders of radii R_i (inner cylinder) and R_o (outer cylinder). The length of this annular enclosure is L_a and it is

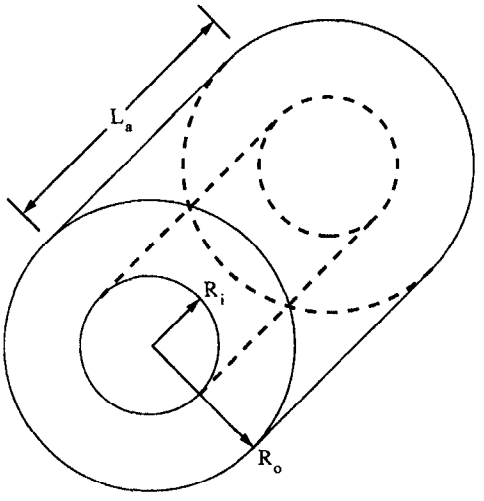

FIG. 1. A schematic sketch of the annular cavity considered in the present study.

closed at both its axial ends. The natural convection flow is driven by the temperature difference between the hot inner cylinder ($T = T_i$) and the cold outer cylinder ($T = T_o$). The axial end walls of the annulus are assumed to be adiabatic.

Using the Boussinesq approximation for the density variation in the buoyancy term, the time-averaged Reynolds equations governing turbulent natural convection in the annular enclosure, using indicial notation are written as:

continuity:

$$u_{j,j} = 0, \tag{1}$$

momentum:

$$\sqrt{\frac{Ra}{Pr}}\,u_j u_{i,j} = \quad p_{,i} - \sqrt{\frac{Ra}{Pr}}\,g_i T + [\mu_{\text{eff}}(u_{i,j} + u_{j,i})]_{,j}, \tag{2}$$

energy:

$$\sqrt{Ra\,Pr}\,u_j T_{,j} = (\lambda_{\text{eff}} T_{,j}]_{,j}, \tag{3}$$

K.E.:

$$\sqrt{\frac{Ra}{Pr}}\,u_j k_{,j} = \left(\frac{\mu_t}{\sigma_k} k_{,j}\right)_{,j} + \frac{\mu_t}{Pr_t} g_j T_{,j} + \mu_t \Phi - \sqrt{\frac{Ra}{Pr}}\,\varepsilon, \tag{4}$$

dissipation:

$$\sqrt{\frac{Ra}{Pr}}\,u_j \varepsilon_{,j} = \left(\frac{\mu_t}{\sigma_\varepsilon}\varepsilon_{,j}\right)_{,j} + c_1(1-c_3)\frac{\varepsilon}{k}\frac{\mu_t}{Pr_t} g_j T_{,j} + c_1 \frac{\varepsilon}{k}\mu_t \Phi - \sqrt{\frac{Ra}{Pr}}\,c_2 \frac{\varepsilon^2}{k}. \tag{5}$$

All variables in the above equations are non-dimensionalized as follows (superscripts have been dropped for convenience):

$$x_i^* = \frac{x_i}{L} \quad u_i^* = \frac{u_i}{U} \quad T^* = \frac{T - T_o}{T_i - T_o} \quad p^* = \frac{pL}{\mu U}$$

$$k^* = \frac{k}{U^2} \quad \varepsilon^* = \frac{\varepsilon}{U^3/L} \quad \Phi^* = \frac{\Phi}{U^2/L^2}.$$

Further:

$$u_t^* = C_\mu \frac{k^{*2}}{\varepsilon^*}\sqrt{\frac{Ra}{Pr}} \quad \mu_{\text{eff}}^* = 1 + \mu_t^*$$

$$\lambda_t^* = \frac{\mu_t^*}{Pr_t} Pr \quad \lambda_{\text{eff}}^* = 1 + \lambda_t^*,$$

and L = the gap width of the annulus $= R_o - R_i$, and $U = (\alpha/L)\sqrt{Ra\,Pr}$, are the characteristic length and velocity, respectively. The values of the constants that appear in the governing equations are: $c_1 = 1.44$, $c_2 = 1.92$, $c_3 = 1.44$, $c_\mu = 0.09$, $Pr_t = 1.0$, $\sigma_k = 1.0$ and $\sigma_\varepsilon = 1.3$. These values are based on the turbulence model proposed by Fraikin *et al.* [24]. Excluding c_3, all the above constants are well-established from data obtained for turbulent forced convection flows. Hence, we have not made an attempt to change these constants even though preliminary studies showed that these constants had a negligible influence on the present results. Therefore, the same constants were used throughout our study and for all the comparisons. A sensitivity analysis of c_3 alone was carried out since this constant influences the buoyancy term in the ε equation. The results of this analysis revealed very little change in the Nusselt number and flow variables with a significant variation of c_3.

Turbulence model

The main challenge associated with the simulation of turbulent flows using the k–ε model is the resolution of sharp gradients of the flow variables in the near-wall region. A large number of grid points would be required in the viscous sublayer close to solid boundaries. This leads to a tremendous increase in CPU time and storage. Another difficulty stems from the fact that the standard k–ε approach (essential to model the high Reynolds number flow in the core region) cannot be used to model the effects of viscosity on the turbulence field in the viscous sublayer (the low Reynolds number effects on turbulence).

Ciofalo and Collins [25] have presented a critical review of different wall treatments presented in conjunction with the k–ε model. Traditionally, the basic approaches to the near-wall modeling are: (i) wall functions to match the viscous sublayer with the outer turbulent flow; (ii) low Reynolds number k–ε model to compute the turbulent viscosity in the near-wall region; and (iii) multizone modeling, i.e. using a one-equation model near the wall and a two-equation model away from it.

In the scheme used in the present work, the fully turbulent outer flow field and the physical boundary are "bridged" by using a single layer of specialized wall elements. The interpolation functions in these

wall elements are based on universal near-wall profiles. They are functions of the characteristic turbulent Reynolds numbers which accurately resolve the local flow and temperature profiles. The turbulent diffusivity in the near-wall region is calculated by using Van Driest's mixing length approach. The standard k–ε equations are solved in the part of the computational domain excluding the wall element region. The elliptic form of the mean conservation equations are solved throughout the computational domain. However, the k–ε model is applied only up to and excluding the wall elements. The application of the present approach to complicated forced flows involving strong and subtle flow reversal has already been demonstrated by Haroutunian and Engelman [26]. The resulting model was found to be more accurate and computationally more effective than the k–ε model using standard wall functions. A brief description of this model is given below.

As mentioned before, the viscosity-affected region between the wall and the fully turbulent region away from the wall is represented by means of a single layer of special elements. These specialized shape functions which are based on universal near-wall velocity profiles accurately resolve the velocity profiles near the wall. The functional form used for the wall element is that given by Reichardt [27]:

$$u^+ = f_R(y^+) = \frac{1}{\kappa}\ln(1+0.4y^+) + 7.8\left[1-\exp\left(-\frac{y^+}{11}\right)-\frac{y^+}{11}\exp(-0.33y^+)\right]. \quad (6)$$

The univeral profile used for temperature takes the following form:

$$T^+ = f_T(y^+, Pr, Pr_t) = Pr\,D_T u^+ + Pr_t(1-D_T)(u^+ + P_T), \quad (7)$$

where

$$D_T = \exp\left(-\frac{y^+}{11}R_T^a\right): \quad a = \begin{cases} 1.1 \rightarrow R_T < 0.1 \\ 0.333 \rightarrow R_T \geqslant 0.1 \end{cases}, \quad (8)$$

$$R_T = \frac{Pr}{Pr_t}, \quad (9)$$

and P_T, based on the Jayatilleke correlation [28], is given by:

$$P_T = 9.24(R_T^{0.75}-1)[1+0.28\exp(-0.007R_T)]. \quad (10)$$

The interpolation functions in the specialized elements are constructed using a tensor product of the one-dimensional basis functions corresponding to the local coordinate directions in the element. The basis functions in the direction along the wall are the same as the elements in the rest of the computational domain. In the direction normal to the wall, the interpolation functions are based on equations (6)–(10).

Boundary conditions

Since the flow is expected to be symmetric about the vertical plane of the annulus, only one-half of the annulus in the angular direction was considered in the present simulation. To allow sufficient resolution in the axial direction, only half the length of the annulus was considered. The flow field and temperature distribution are expected to be symmetric about the mid-axial symmetry plane. The validity of this assumption about the mid-axial plane was further verified by simulating the entire annular domain. It was observed that the symmetry condition is justified. No exchange of energy occurs across the symmetry planes. The boundary condition applied here therefore requires that the normal velocity, i.e. the angular velocity for the angular symmetry plane and the axial velocity for the mid-axial symmetry plane be zero. Gradients of the remaining variables: radial velocity, axial velocity, temperature, kinetic energy and dissipation are assumed to be zero at the symmetry planes. At all solid walls of the cavity, the no-slip boundary condition for velocity is applied. The inner and outer cylinders are isothermal whereas the axial end walls are insulated. As mentioned earlier, in the wall elements immediately next to the solid walls of the cavity, the k and ε equations are not solved. Hence, boundary conditions for these variables are applied at the first grid point away from the wall. These are:

$$\left.\begin{aligned} \frac{\partial k}{\partial n} &= 0 \\ \varepsilon_P &= \frac{(c_\mu k)^{1.5}}{\kappa\Delta} \end{aligned}\right\} \text{ at the first grid point away from the wall.}$$

This boundary condition for k plays an important role in the approach used here. It allows the value of k to adjust in response to the turbulence processes in both local and neighboring regions.

Numerical scheme

The discretization of the set of governing equations (1)–(5) along with the boundary conditions was carried out by using a finite element formulation based on the Galerkin method of weighted residuals. This results in a highly non-linear, coupled system of algebraic equations. This system of equations was then solved by using an iterative solution scheme based on the segregated solution algorithm. Basically, this scheme involves decomposition of the entire system of equations into smaller subsystems. Each subsystem is then solved by using an iterative solver. Convergence was assumed to have been reached when the relative change in variables between consecutive iterations was 10^{-3}. In addition, heat imbalance allowed between the inner and outer cylinders was found to be negligible for each case. Computations

were carried out on the Cray YMP Supercomputer and Silicon Graphics IRIS (R4000) workstation.

Heat transfer results

Heat transfer results are presented in terms of the Nusselt number which is defined as the ratio of the actual heat transfer rate to the pure conduction heat transfer rate. Thus the expressions for the Nusselt number over the inner and outer cylinders, respectively, are given by:

$$Nu_i = R_i \ln\left(\frac{R_o}{R_i}\right)\left.\frac{\partial T}{\partial r}\right|_{r=R_i},$$

$$Nu_o = R_o \ln\left(\frac{R_o}{R_i}\right)\left.\frac{\partial T}{\partial r}\right|_{r=R_o}.$$

A second-order accurate three-point differencing scheme was used to calculate the Nusselt number results. The mean Nusselt number is obtained by integrating the local Nusselt number over the inner or outer cylinders.

RESULTS AND DISCUSSION

In the present work, results obtained using both a two-dimensional as well as a three-dimensional model are described. Detailed parametric studies were made using the two-dimensional model. The effects of the governing dimensionless parameters, namely the Rayleigh number and Prandtl number, on the flow and temperature distributions in the annulus were thoroughly examined. The influence of geometric parameters such as the radius ratio was studied in detail. Majority of the results presented here are for an inner cylinder temperature of $T_i = 1$, an outer cylinder temperature of $T_o = 0$, radius ratio equal to 2.6 and using air ($Pr = 0.7$) as the working fluid. These values were chosen so as to facilitate comparisons with available experimental data. For each case studied here, the characteristic velocity scale based on $Ra = 10^6$ and $Pr = 0.7$ was used to present the non-dimensional results. Heat transfer results are presented by means of plots showing the Nusselt number variation with the angular position, where the angle (degrees) is measured from the bottom angular position of the annulus. For the three-dimensional results, the axial location was measured from the solid wall of the annulus, i.e. $z = 0$ at the solid wall.

As part of the solution strategy, results were first obtained for the laminar regime up to a Rayleigh number of 10^5. The laminar results had already been validated in a previous study [30]. These results have been compared with previous experimental and numerical data of Takata *et al.* [5] and Vafai and Ettefagh [7]. To obtain the results for $Ra = 10^6$ and higher, the turbulence model discussed in the previous section was utilized. The flow and temperature fields obtained for $Ra = 10^5$ were used as an initial estimate. For the turbulence variables, i.e. the turbulent kinetic energy and turbulent dissipation, it was found that some amount of experimentation was required to provide a good initial guess. The initial guess had a crucial effect on the time required in achieving converged solutions. It should be noted that non-zero values of these variables were essential in initiating the turbulent flow calculations. An under-relaxation factor of 0.5 and streamline upwinding was used for all the variables. However, it should be noted that the initial guess had no effect on the final converged result.

Grid-size independence and comparison against experimental results

The two-dimensional model was based on the assumption that the annulus is long enough so that axial effects can be neglected. Hence motion is confined to the radial plane and the z-direction dependence is removed from the problem. A detailed grid independence study was carried out on the two-dimensional model. Preliminary results were obtained using a 41×41 mesh comprised of linear elements. A variable mesh grading was used in both the angular and radial directions for all grid distributions, such that the mesh size at the boundaries was half of the mesh size at the center of the computational domain. To confirm that the mesh used was sufficiently fine, results were then obtained by increasing the grid points to 61 in both directions. A comparison of magnitudes of velocity, turbulent kinetic energy and turbulent viscosity showed that these values changed by less than 1%. The temperature fields were also in good agreement. However, a comparison of the Nusselt numbers from the two cases showed some change. Since this was not acceptable, another run was made using a 81×81 mesh. It was observed that the flow and temperature fields remained unchanged and further, the maximum change in the Nusselt number was approximately 1%, thus indicating that results were now independent of the grid size. The Nusselt number variation over both cylinders as a function of the angular position for different mesh sizes is shown in Fig. 2.

Since no experimental data under standard pressure conditions were available for the present configuration, a rough comparison of the present results with some experimental results corresponding to a high pressure system were made. To this end, the inner and outer cylinder Nusselt number results were compared against some of the experimental results of Kuehn and Goldstein [17], as shown in Fig. 3. Nusselt numbers over the inner and outer cylinders compared against their experimental data are shown in Fig. 3. The Nusselt number values obtained by Farouk and Guceri [20] are also shown in this figure. The 61×61 mesh with 3-point differencing (represented by the solid line in the graph) is used to determine the Nusselt number values in the present study. Numerical results for $Ra = 10^6$ were compared against the experimental results of Kuehn and Goldstein [17] for $Ra = 8.02 \times 10^6$ and 2.51×10^6. The 61×61 mesh using 3-point differencing (solid line in Fig. 3) was

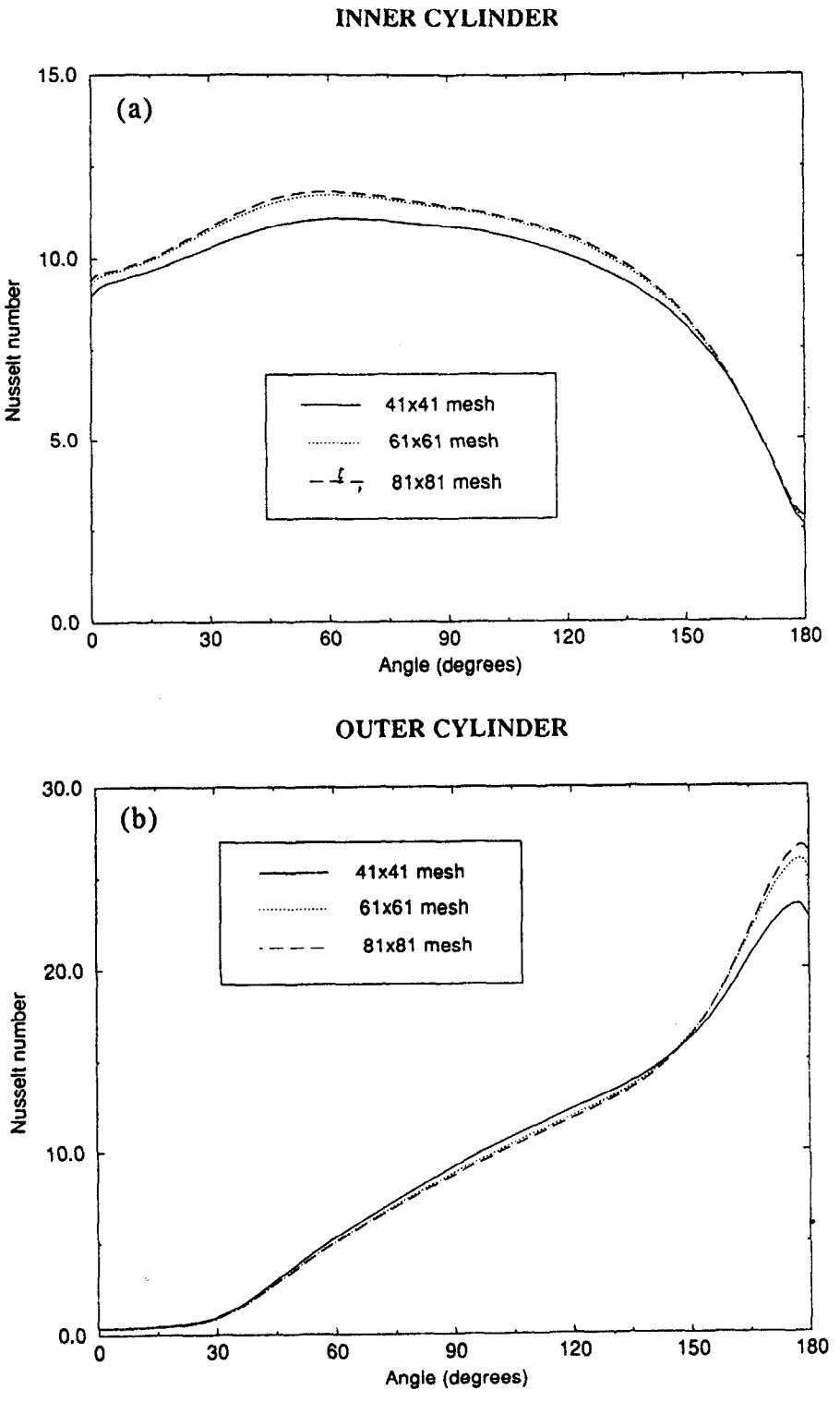

FIG. 2. Grid-size independence of Nusselt number values—$Ra = 10^6$, $Pr = 0.7$ and $R_o/R_i = 2.6$: (a) inner cylinder; and (b) outer cylinder.

used to present the heat transfer results. As seen from the figure, the numerical results obtained in the present study over-predict the heat transfer rates over the experimental results. This difference (9% maximum) could be as a result of the fact that the experiments of Kuehn and Goldstein [17] were carried out for pressurized nitrogen. Though the Prandtl number is the same in both cases, it should be noted that the high pressure during the experiments could change the physical processes underlying this phenomenon.

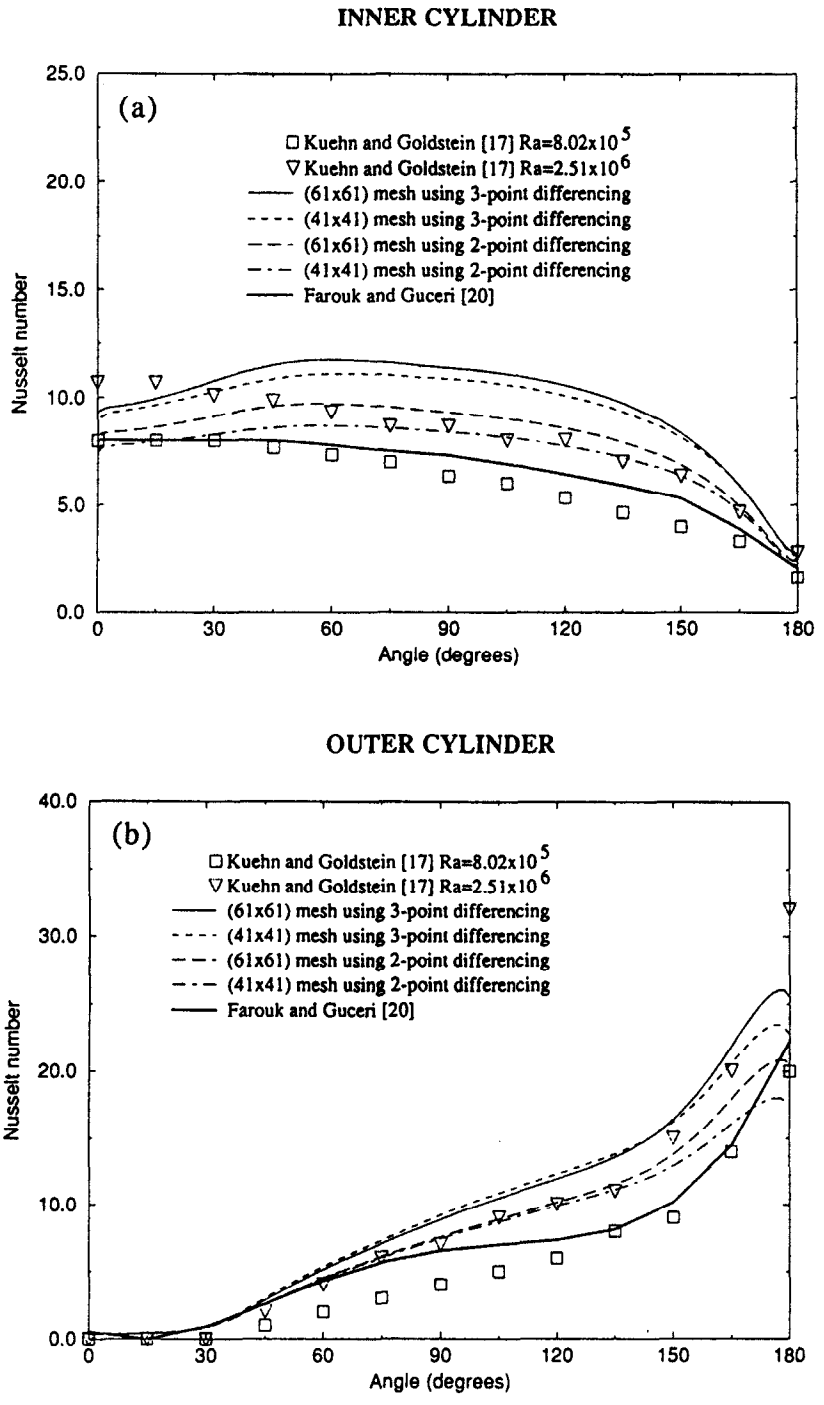

FIG. 3. Comparison of present results using different methods against experimental data of Kuehn and Goldstein [17] and Farouk and Guceri [20]—$Ra = 10^6$, $Pr = 0.7$ and $R_o/R_i = 2.6$: (a) inner cylinder; and (b) outer cylinder.

Furthermore, the energy equation in the present form is valid only for gases at low pressures.

Farouk and Guceri [20] have presented a similar comparison of their numerical results against the experimental data of Kuehn and Goldstein [17]. Their results showed better agreement with the experimental data. This was puzzling since the temperature field presented by them showed good qualitative agreement with our results. We have used a 3-point differencing scheme for obtaining the Nussselt number results at both the inner and outer cylinders. Farouk and Guceri [20] do not discuss the method used to determine the Nusselt number values. In addition, there is no mention of grid-size independence being established

in their work, where they used a relatively coarser mesh (41×51) to obtain their results. We therefore experimented with different methods and different mesh sizes to study the influence of the differencing scheme on the Nusselt number results. The best comparison with the experimental results was obtained when a 41×41 mesh with a 2-point differencing was used to obtain the Nusselt number results. However, it was observed that grid-size independent Nusselt number values could not be obtained when 2-point differencing was used. Further, the magnitude of the truncation error is much lower when 3-point differencing is used. All Nusselt number values presented here are therefore obtained using the 3-point differencing scheme.

It was observed that heat transfer rates increase gradually from the bottom of the inner cylinder up to about 60°. The Nusselt number value reaches a peak and then decreases continuously till the top of the inner cylinder. This behavior can be explained as follows. At high Rayleigh numbers, the center of rotation of the recirculating eddy moves upward in the annular cavity. Hence, the stagnation point on the inner cylinder moves to 60° from the bottom angular plane. This is the reason for the increase in the Nusselt number along the inner cylinder initially in the bottom portion. The minimum heat transfer rate is at the top angular position because of the boundary-layer separation. The heat transfer rates along the outer cylinder, on the other hand, show a continuous increase from the bottom to the top angular position.

As a further test of the accuracy of the numerical results obtained in the present study, the time-averaged temperature distribution within the cavity was compared for a radius ratio of 2.6, $Pr = 0.7$ and $Ra = 2.51 \times 10^6$ against the experimental results of Kuehn and Goldstein [17]. Results for the same case were also compared with the numerical results of Fukuda *et al.* [22]. These comparisons are shown in Fig. 4a. The time-averaged temperature profiles are shown at three angular locations for clarity of presentation. The numerical results obtained in the present study show very good agreement with these previously published experimental results. As mentioned in the paper, the discrepancies can be attributed to the fact that the experiments were not carried out under standard pressure conditions. Further, the numerical modeling is based on the assumption of constant thermophysical properties. At high Rayleigh numbers, the temperature differences involved in the process are significant. In reality, thermal conductivity of air increases with an increase in temperature. In the numerical model, a constant thermal conductivity based on the film temperature $(T_h + T_c)/2$ was used. Hence, the numerical model uses a higher thermal conductivity in the lower region (where the actual temperatures of the fluid are lower) of the annulus and a lower thermal conductivity in the upper region of the annulus. This explains the higher temperatures predicted by the numerical model in the lower region of the annulus and lower temperatures in the upper region of the annulus when compared with the experimental data.

An additional source of comparison is the experimental study of turbulent natural convection of helium in a horizontal annulus at cryogenic temperatures performed by Bishop [18] and McLeod and Bishop [19]. Numerical runs were carried out to simulate the conditions under these experiments. Wherever possible, comparisons are also presented with results from the numerical simulations of Fukuda *et al.* [22]. Figure 4b and c shows comparisons of time-averaged temperature profiles against these previous experimental and numerical results. It is apparent from these figures that the results obtained using the present model are in good agreement with the experimental results. As mentioned above, the minor discrepancies could arise from the fact that the constant property assumption is not a very accurate one at high Rayleigh numbers due to the high temperature differences involved.

Effect of Rayleigh number

Figures 5–7 depict the streamlines, isotherms, turbulent kinetic energy contours and dissipation contours for $Ra = 10^6$–10^8 for the nominal radius ratio (2.6) and $Pr = 0.7$. As seen from these figures, the time-averaged mean flow field exhibits the recirculating kidney-shaped pattern at these higher Rayleigh numbers. The basic structure of the flow field is found to be composed of: the increase in the thickness of the thermal boundary layer along the inner cylinder; the rise of the hot buoyant plume toward the top of the outer cylinder; entrainment of the buoyant plume into the thermal boundary layer along the outer cylinder; and finally the separation of the boundary layer from the outer cylinder to complete the recirculation pattern inside the cavity. The turbulent kinetic energy contours indicate high turbulence levels near the top of the outer cylinder and near the center of rotation of the recirculating flow. For the Rayleigh numbers considered, the turbulent viscosity is found to be maximum near the center of rotation indicating that the Reynolds stress assumes a large value in this region.

As the Rayleigh number increases, the separation point of the inner cylinder boundary layer moves upward causing the isotherms to cluster to a greater extent around the inner cylinder circumference. The center of rotation of the recirculating flow pattern moves toward the vertical symmetry plane and the boundary layers along the inner and outer cylinders are much thinner. From the values of the turbulent viscosity and turbulent kinetic energy within the cavity, it can be seen that, as expected, the turbulence intensities within the cavity increase with an increase in Rayleigh number.

The increased strength of the convective flow in the cavity is expected to manifest itself into increased heat transfer rates inside the cavity. This can be seen from

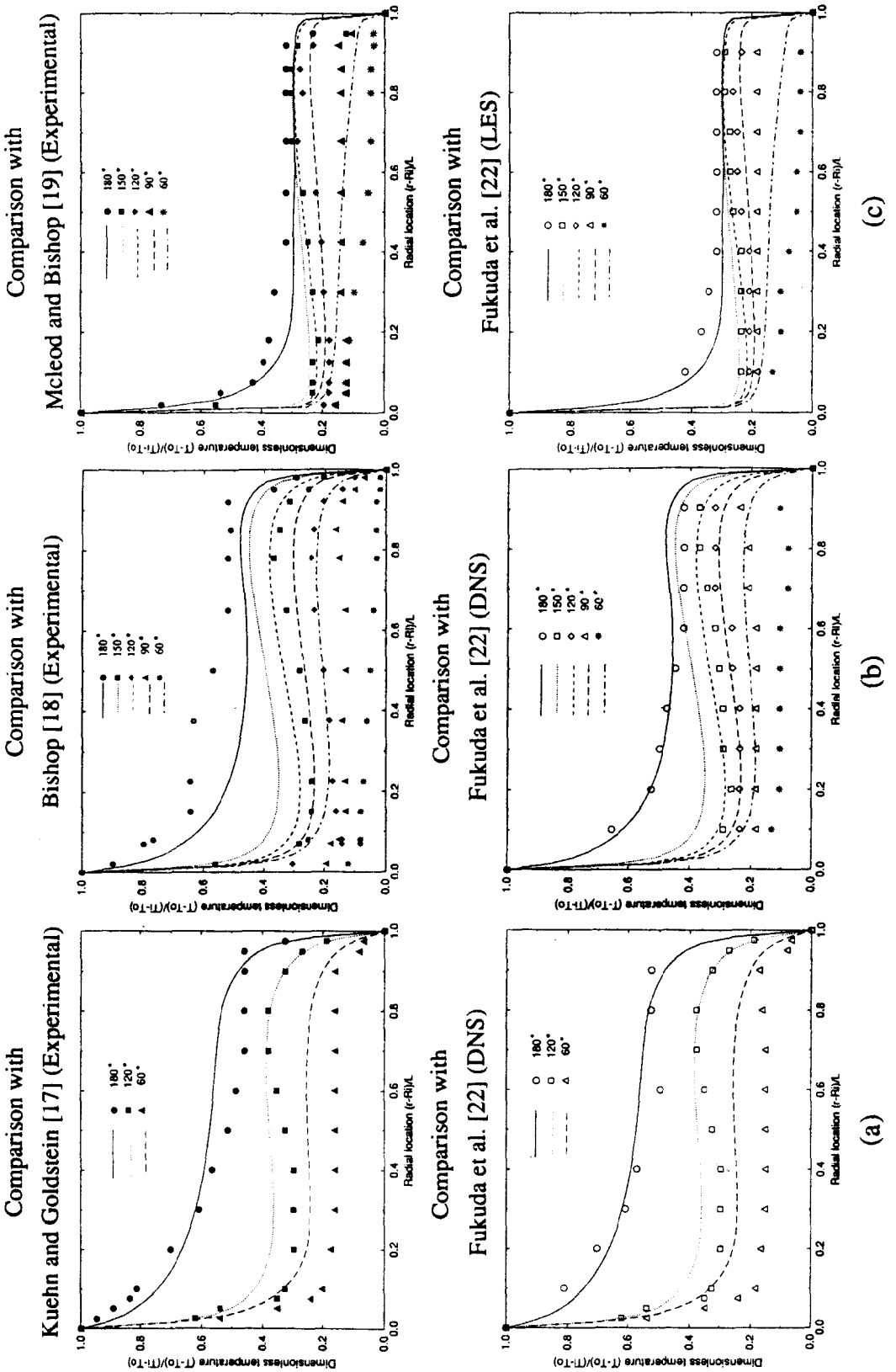

Fig. 4. Comparison of results against previous experimental and numerical results: (a) $Ra = 2.51 \times 10^6$, $Pr = 0.7$ and $R_o/R_i = 2.6$; (b) $Ra = 1.3 \times 10^7$, $Pr = 0.688$ and $R_o/R_i = 3.36$; and (c) $Ra = 1.18 \times 10^9$, $Pr = 0.688$ and $R_o/R_i = 4.85$.

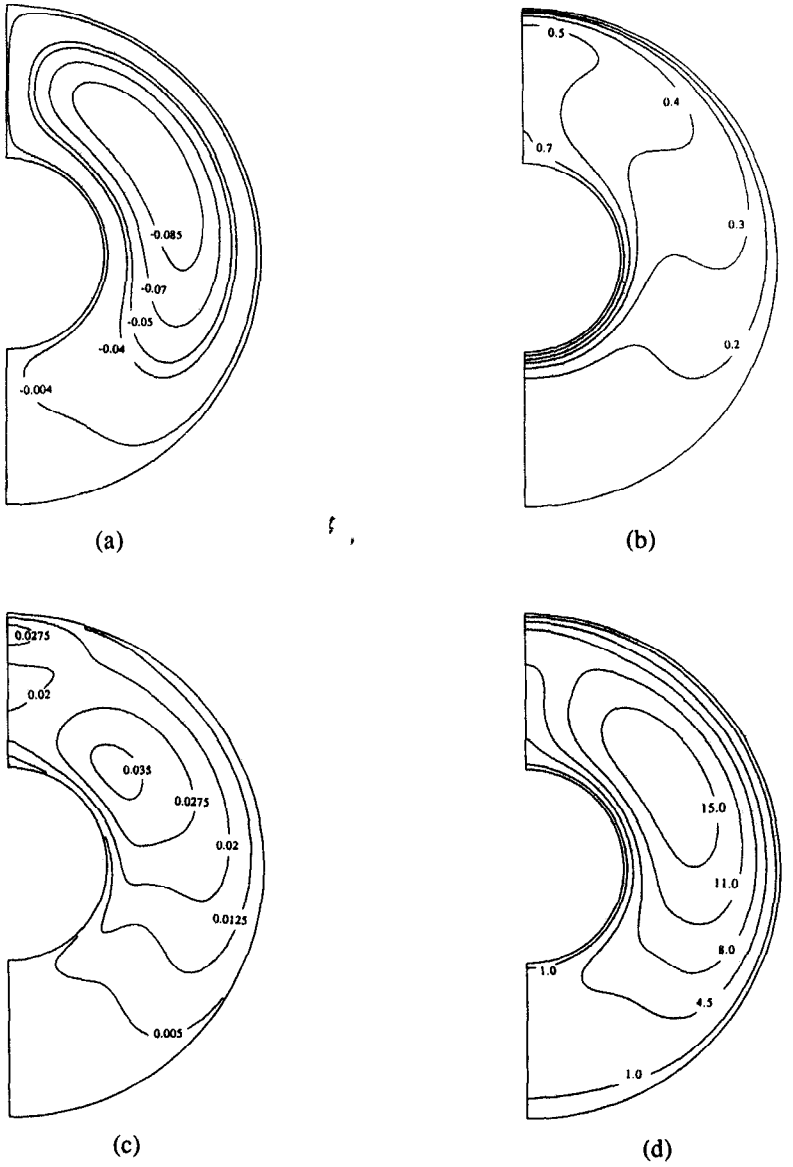

FIG. 5. Time-averaged turbulence variables—$Ra = 10^6$, $Pr = 0.7$ and $R_o/R_i = 2.6$: (a) streamlines; (b) isotherms; (c) turbulent K.E.; and (d) turbulent viscosity.

the graphs presented in Fig. 8, where Nusselt number results are presented for the range of Rayleigh numbers considered here. It can be observed that the delayed boundary-layer separation at the inner cylinder surface causes the heat transfer rates to be more uniform at higher Rayleigh numbers except in the region at the top where the buoyant plume separates from the inner cylinder. The heat transfer rates at the outer cylinder maintain the increasing trend from the bottom to the top of the outer cylinder. However, the magnitudes are considerably higher because of the stronger convective flow at higher Rayleigh numbers.

Effect of Prandtl number

Flow of air ($Pr = 0.7$) in an annulus with $R_o/R_i = 2.6$ becomes turbulent at approximately $Ra = 10^6$. The results for this geometry and fluid have aleady been presented in the previous sections. Additional calculations were made for an annulus with the same dimensions and containing fluids with $Pr = 0.01$, 7, 100, 1000 and 5000 to study the effect of this thermophysical property on the flow and heat transfer characteristics. The transition to turbulence is expected to occur at a later stage for fluids having higher Prandtl numbers. Results are presented for a radius ratio of 2.6 at $Ra = 10^8$, i.e. at the higher end of the Rayleigh number spectrum. The variable field at the lower Prandtl number was used as an initial guess to obtain the solution for the higher Prandtl numbers. The turbulent viscosity was found to decrease with an increase in Prandtl number, thus indicating lower levels of turbulence at the same Ray-

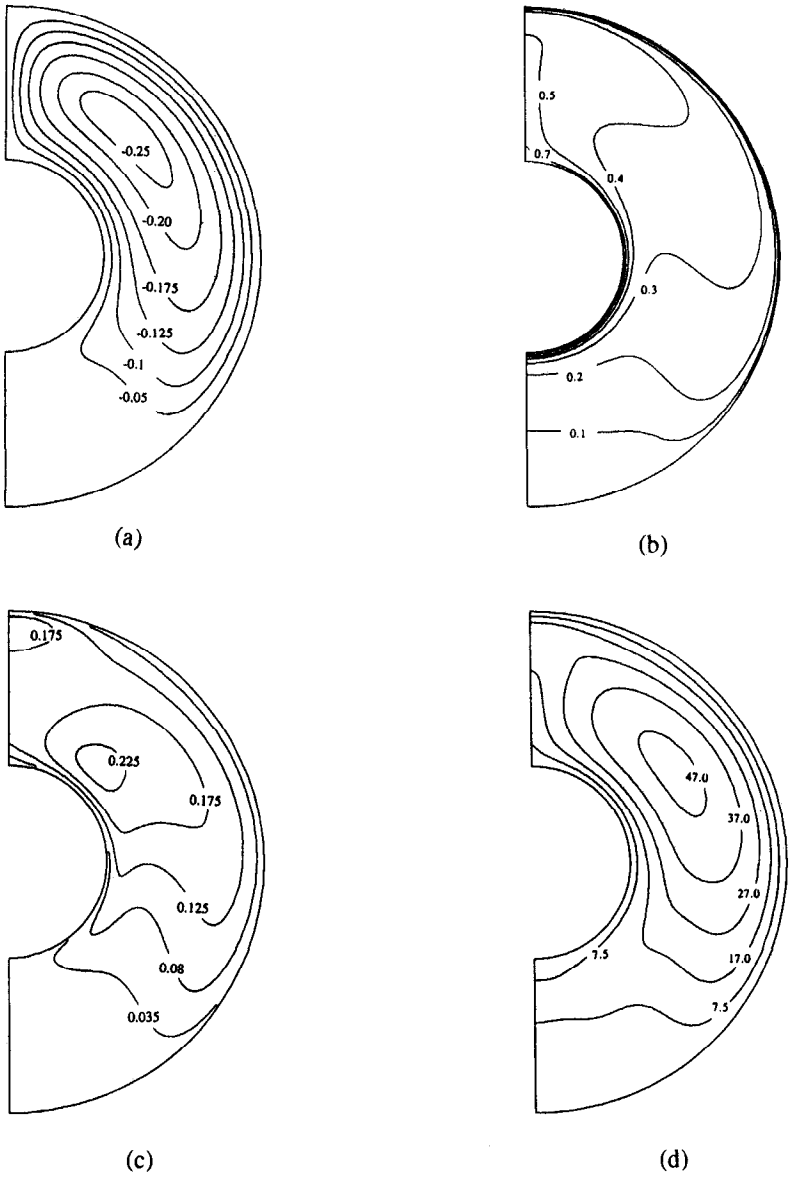

FIG. 6. Time-averaged turbulence variables—$Ra = 10^7$, $Pr = 0.7$ and $R_o/R_i = 2.6$: (a) streamlines; (b) isotherms; (c) turbulent K.E.; and (d) turbulent viscosity.

leigh number (e.g. the maximum turbulent viscosity was found to be 2944 for the $Pr = 0.01$ case and 4.2 for the $Pr = 100$ case).

An interesting phenomenon was observed for the $Pr = 0.01$ case. The natural convection flow field within the cavity was found to be a combination of two recirculation loops of equal strength which combine with each other at approximately the 90° angular position of the cavity. Basically, as fluid rises along the inner cylinder, part of it separates at the mid-angular (90°) position of the inner cylinder and gets entrained into the outer cylinder boundary layer. whereas the rest of the fluid continues on its upward path, separates near the top of the inner cylinder and impinges on the top of the outer cylinder (not shown here for brevity). The early separation is due to the fact that the fluid inertia is not enough to withstand the adverse pressure gradient due to the curvature of the inner cylinder. This bicellular flow was more apparent at lower Rayleigh numbers. At $Ra = 10^8$, these two cells have combined to form a single loop within the cavity (Fig. 9a). Furthermore, a weak cell (rotating opposite to the global recirculation loops) was observed at the bottom of the cavity. The formation of these cells is consistent with observations from previous experimental and numerical results pertaining to liquid metal natural convection flow in rectangular cavities (Wolff *et al.* [31]). The isotherms in Fig. 9a indicate the influence of this flow field structure on the temperature distribution within the cavity. The temperature gradients are found to be lowest at the top of the inner cylinder and at the bottom of the

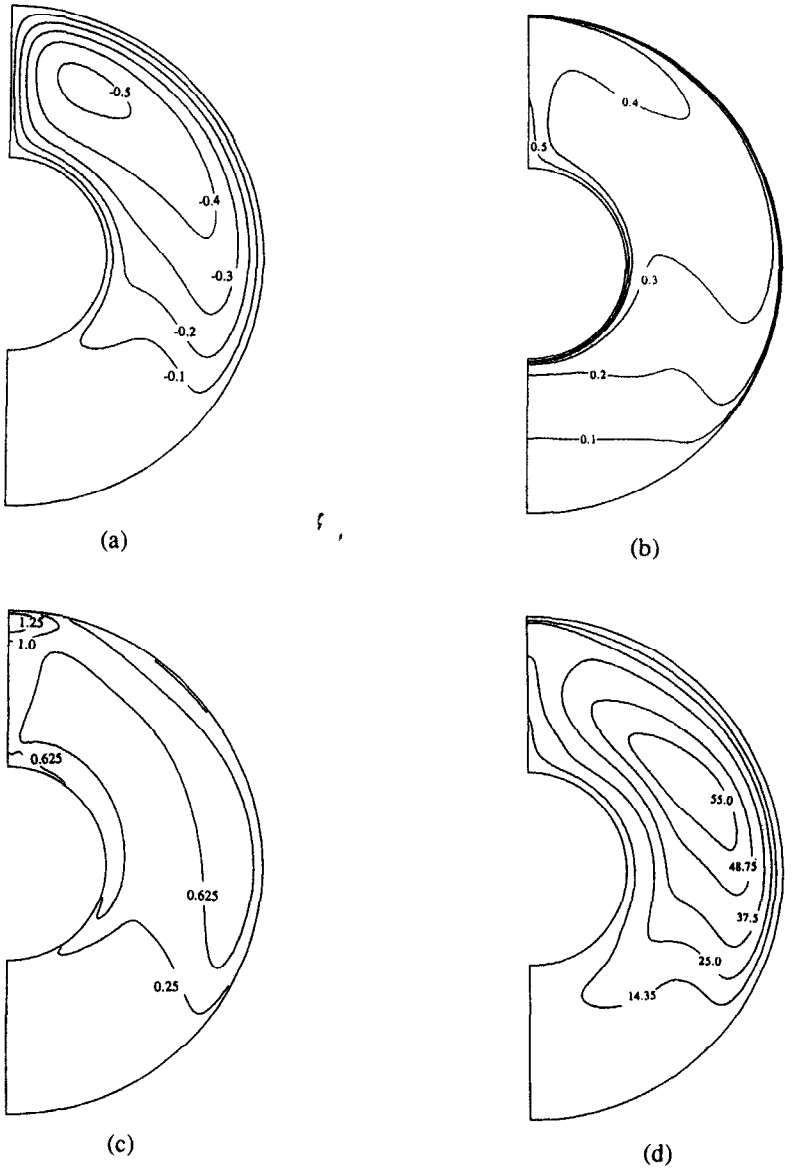

FIG. 7. Time-averaged turbulence variables—$Ra = 10^8$, $Pr = 0.7$ and $R_o/R_i = 2.6$: (a) streamlines; (b) isotherms; (c) turbulent K.E.; and (d) turbulent viscosity.

outer cylinder. Due to the weak recirculation at the bottom of the cavity, the gradients are also quite low at the bottom of the inner cylinder. The isotherms are clustered around the inner cylinder at approximately the 30° angular position. Also, temperature gradients are found to be high at the 90° angular position for the outer cylinder.

For $0.01 < Pr < 100$, comparison of streamlines at different Prandtl numbers (Figs. 9 and 10a) shows that the strength of the natural convective flow field increases as the Prandtl number increases, since the buoyancy parameter $(g\beta/\alpha\nu)$ is higher for higher Prandtl number fluids. Hence, the boundary layer separation along both surfaces (near the top of the inner cylinder and at the bottom of the outer cylinder) gets delayed. Comparison of isotherms in Fig. 9 and Fig. 10 indicates the existence of a thinner thermal boundary layer along the inner and outer cylinders for the higher Prandtl number cases. The core temperature of the fluid reduces considerably as the Prandtl number increases since the thermal boundary layers are more confined around the inner and outer cylinders. Hence, temperature gradients along the inner and outer cylinders increase as the Prandtl number increases.

Figure 11 clearly shows the effect of Prandtl number in enhancing the heat transfer rates from the inner and outer cylinders for $0.01 < Pr < 100$. The inner and outer cylinder Nusselt numbers continuously increase with an increase in Prandtl number in this range. For $Pr = 1000$, the heat transfer rates are found to be less than for $Pr = 100$ at this Rayleigh number (10^8) because the fluid is in the laminar regime. The

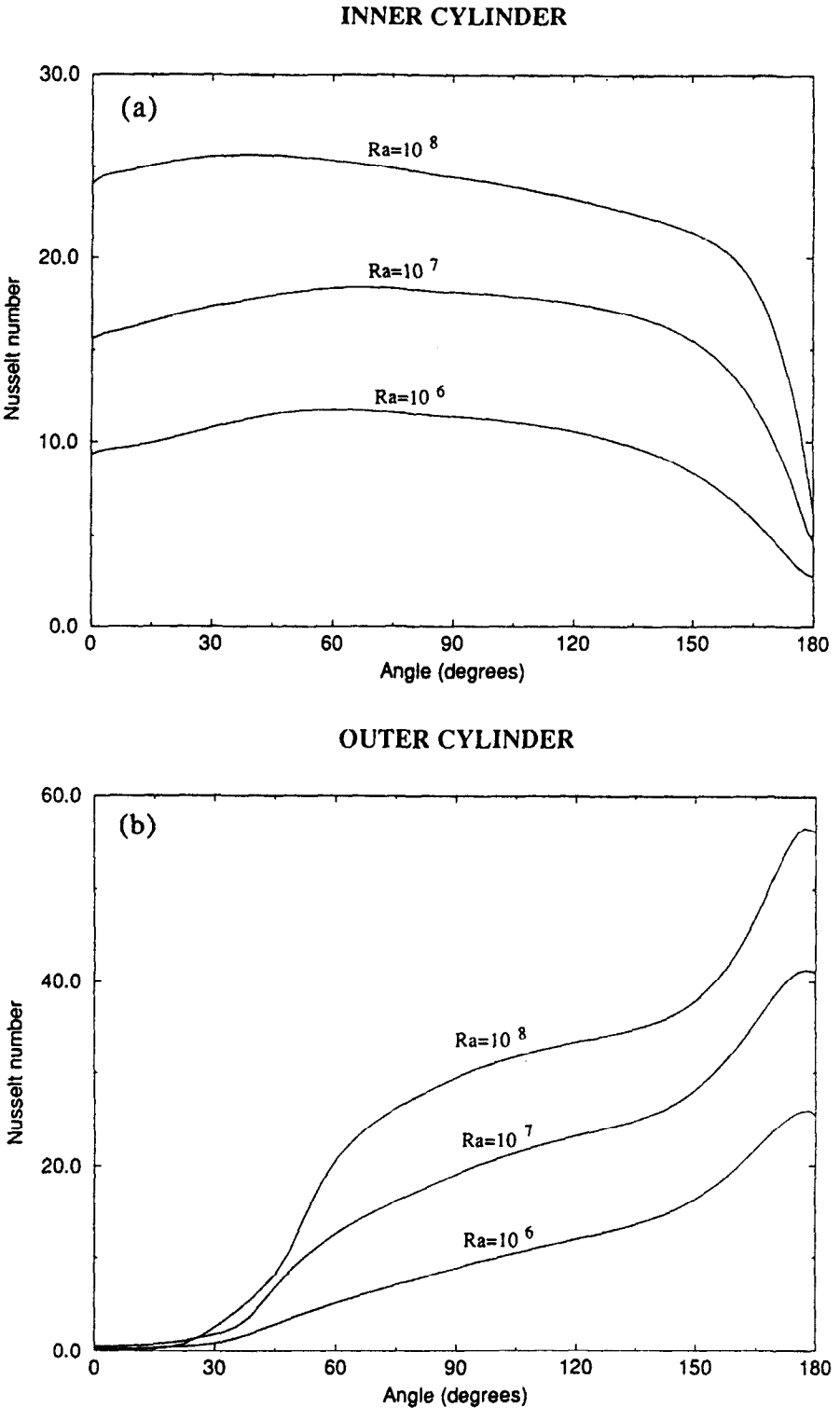

FIG. 8. Nusselt number distribution as a function of Rayleigh number—$Pr = 0.7$ and $R_o/R_i = 2.6$: (a) inner cylinder; and (b) outer cylinder.

Nusselt number for $Pr = 5000$ is only slightly higher than for $Pr = 1000$. A decrease in the inner cylinder Nusselt number was observed at approximately the 60–80° angular position for these fluids. The high strength of the recirculating flow field at high Prandtl numbers results in a temperature inversion very close to the inner cylinder (Fig. 10b and c) thus causing the heat transfer rates to drop at these locations. For $Pr = 0.01$, the low Nusselt numbers at the bottom of the inner cylinder are due to the presence of the weak

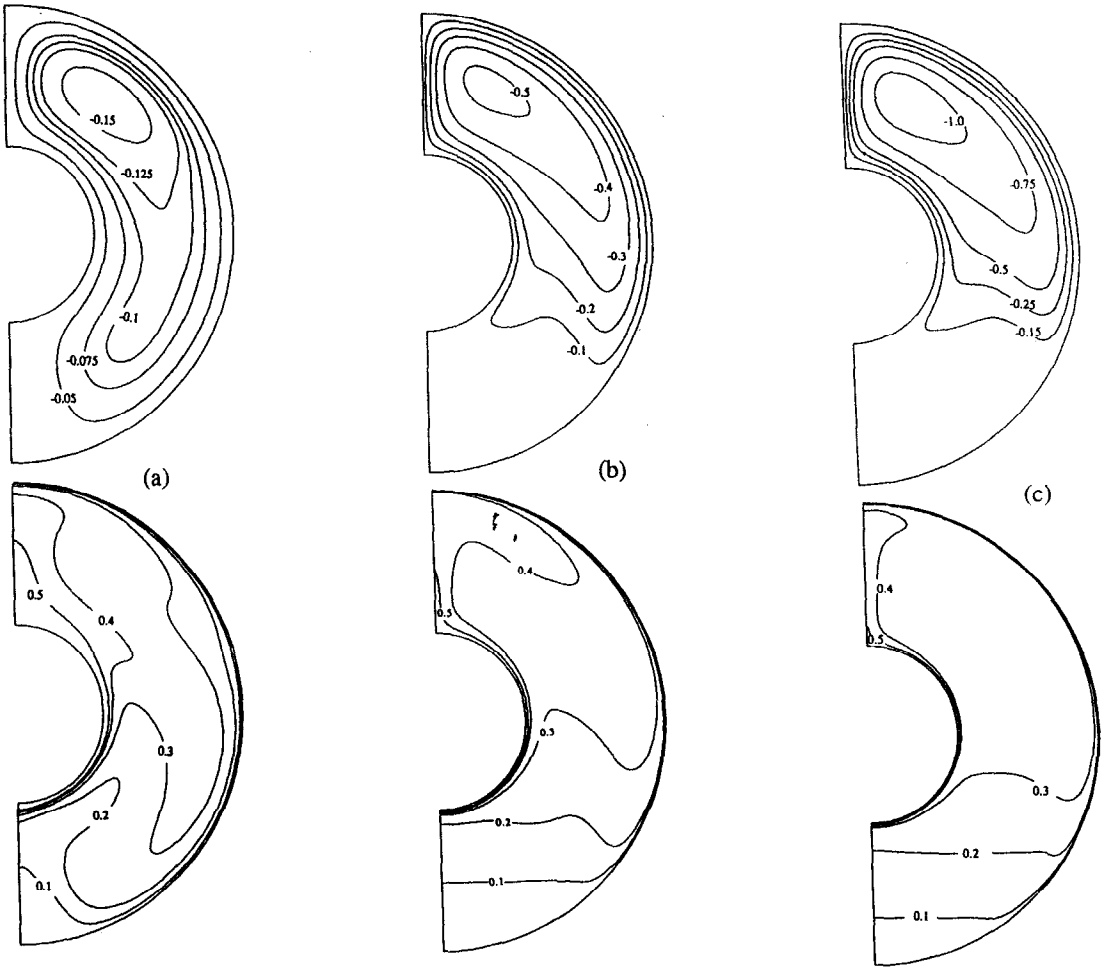

FIG. 9. Streamlines and isotherms at $Ra = 10^8$ and $R_o/R_i = 2.6$: (a) $Pr = 0.01$; (b) $Pr = 0.7$; and (c) $Pr = 7$.

recirculation cell in the bottom of the cavity. For $0.01 < Pr < 100$, the heat transfer rates are considerably uniform over the circumference of the inner cylinder except at the top where the boundary layer separates. This decrease is observed over a shorter length for the higher Prandtl number cases, because of the delayed separation of the plume from the inner cylinder. For the outer cylinder, the boundary-layer effect causes an increase in the heat transfer rates at high Prandtl numbers. In addition, as observed from the Nusselt number distribution for $Pr = 100$, heat transfer from the bottom of the outer cylinder is not negligible, because of the thinner boundary layer along the outer cylinder.

At the top of the outer cylinder, the cross-over observed in the Nusselt number distribution can be explained as follows. Since the bulk temperature of the fluid is higher for the lower Prandtl number case, the buoyant plume rising toward the outer cylinder has a higher mean temperature. This hot fluid rises vertically and impinges on the outer cylinder. Hence the temperature drop experienced by the cavity fluid at the top of the outer cylinder is higher for the lower Prandtl number fluid, resulting in higher heat transfer rates at this location. However, as the fluid moves downward along the outer cylinder boundary layer, the lower bulk fluid temperature causes the Nusselt number to be greater for the higher Prandtl number case. For $Pr = 0.01$, the outer cylinder Nusselt number is found to be higher than for $Pr = 0.7$ and 7 because of the bicellular nature of the flow explained above. The thermal boundary layer along the outer cylinder is thin except in a small region at the bottom of the annulus where fluid separates and moves toward the inner cylinder. For $Pr = 1000$ and 5000, heat transfer from the outer cylinder is negligible in the bottom portion because of the presence of stagnant fluid in this region. The high temperature gradients in the annulus cause the heat transfer rates to be higher at other locations of the outer cylinder. Beyond the 90° angular position in the annulus, the Nusselt number for $Pr = 100$, 1000 and 5000 follow almost identical trends.

Effect of radius ratio (R_o/R_i)

In addition to the Rayleigh number and Prandtl number, which are primary parameters affecting natu-

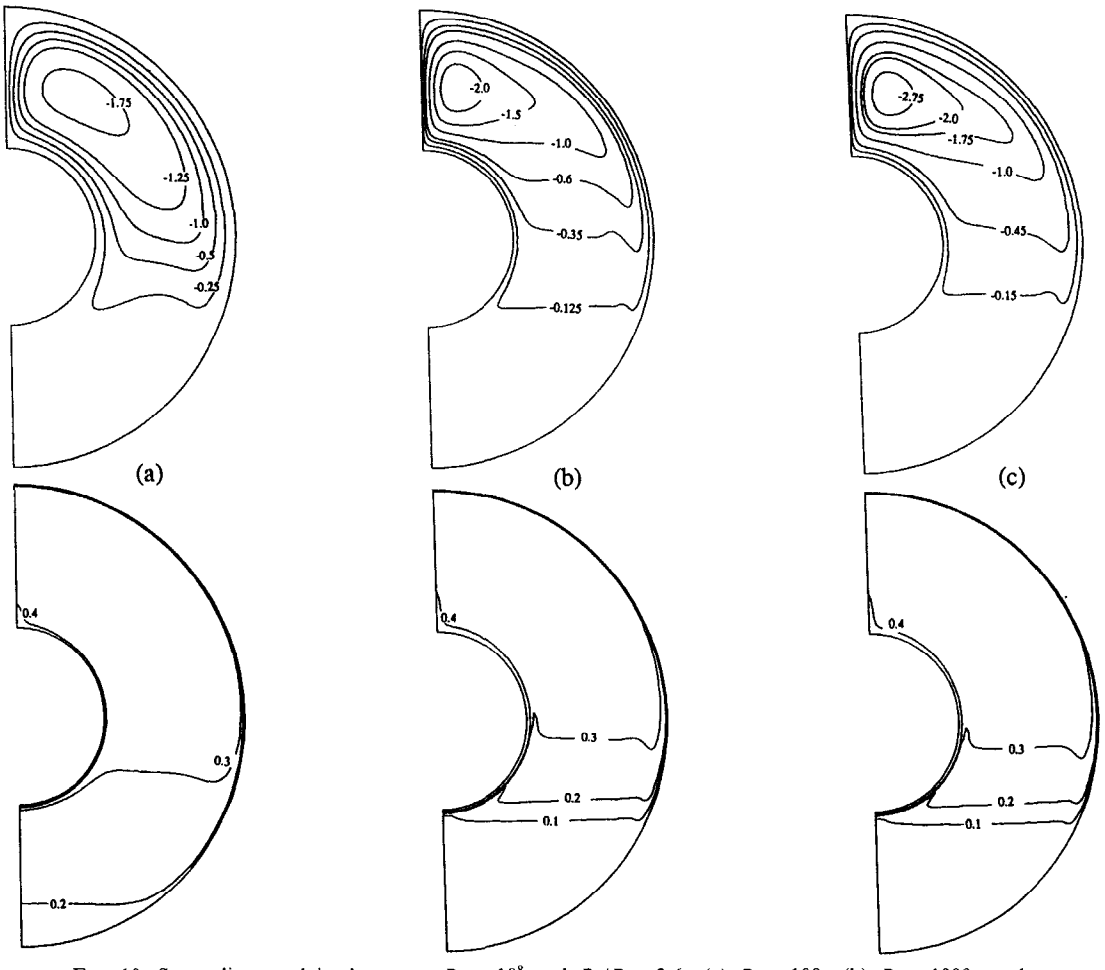

FIG. 10. Streamlines and isotherms at $Ra = 10^8$ and $R_o/R_i = 2.6$: (a) $Pr = 100$; (b) $Pr = 1000$; and (c) $Pr = 5000$.

ral convection in any geometry, another parameter which is critical in buoyancy-induced flows in annuli is the radius ratio of the annulus. This was demonstrated in the experimental studies of Powe *et al.* [33] who classified annular natural convection flow into different regimes based on the value of an inverse gap-width ratio in addition to the Grashof number. In the present study, results were obtained for $R_o/R_i = 1.5, 2.6, 3.5, 6, 9$ and 11 to cover a wide range of geometries.

The isotherms for the cases studied here are shown in Fig. 12 at $Ra = 10^8$ and $Pr = 0.7$. The gap-width has been maintained constant in all cases and the radii of the inner and outer cylinders have been changed to obtain the necessary radius ratio. However, for clarity of presentation, the cavity has been scaled to the same outer cylinder radius. From the temperature distribution within the cavity, it is apparent that the temperature gradients at the inner cylinder increase as the radius ratio increases. The core temperature of the cavity fluid is found to decrease with an increase in the radius ratio. The temperature distribution along the horizontal plane of the annulus is plotted in Fig. 13. The dependence of the core temperature of the annulus on the radius ratio can be clearly seen from this figure. For the same gap-width L, when the radius ratio decreases, the fluid has to travel a greater distance in the cavity to complete the natural convection loop. Hence more heat is transferred to the fluid causing its bulk temperature to rise. This effect is clearly seen in Fig. 13. The core temperature is found to be maximum for $R = 1.5$ and keeps decreasing continuously as the radius ratio increases. Hence, the temperature gradients at the inner cylinder are lowest for the lower radius ratio case. The temperature gradients along the inner cylinder were calculated and this fact was confirmed. However, since Nusselt number is also influenced by the heat transfer area, the Nusselt number for the inner cylinder was higher for the lower radius ratio cases. The Nusselt number distribution for the inner cylinder is shown in Fig. 14a. Therefore, it should be noted that, while the temperature gradient is lowest for the lowest radius ratio, the Nusselt number which is affected by the heat transfer area also is lowest for the highest radius ratio.

For the outer cylinder (Fig. 14b), the same behavior was observed, i.e. the Nusselt number was found to increase with a decrease in the radius ratio except in

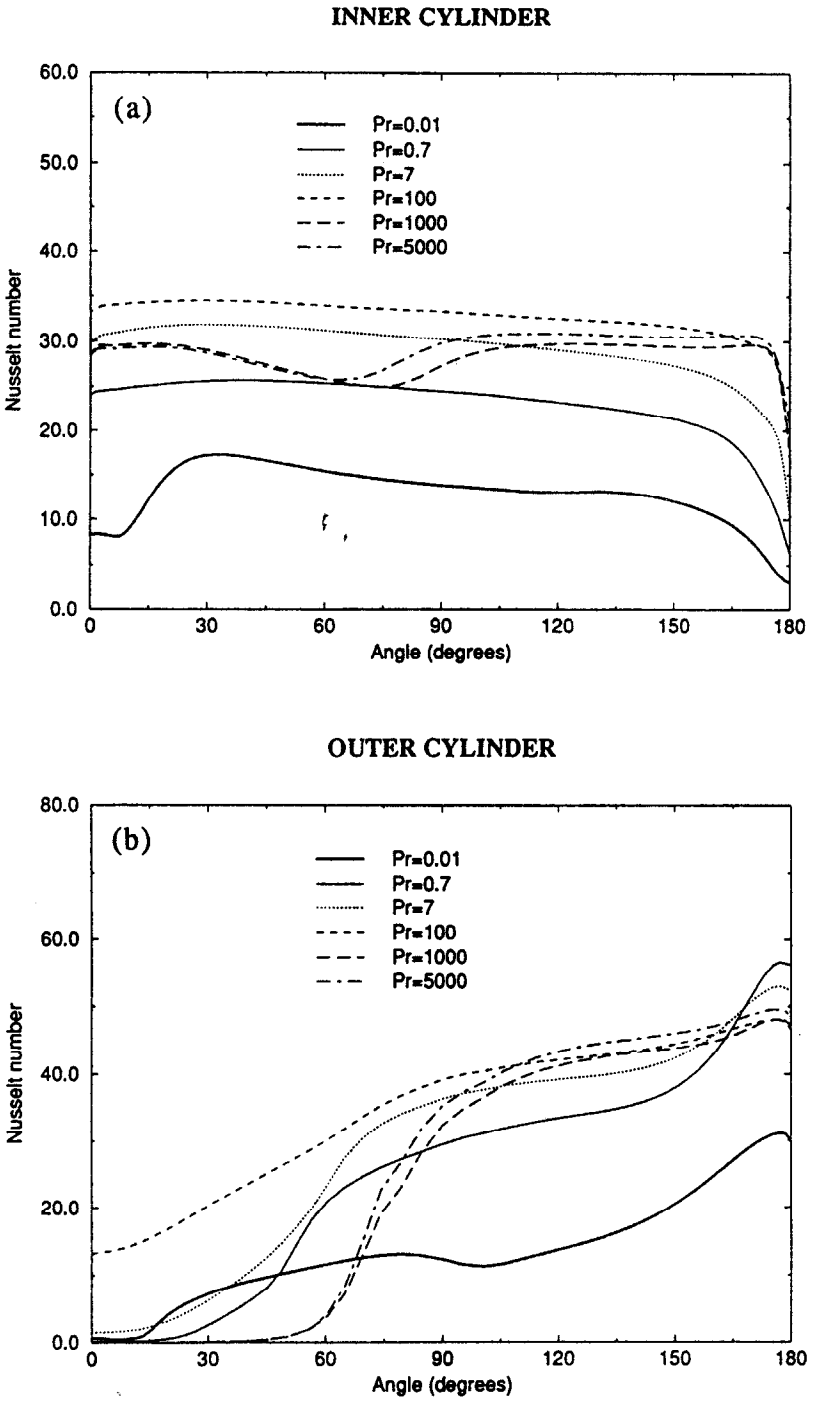

FIG. 11. Nusselt number distribution as a function of Prandtl number—$Ra = 10^8$ and $R_o/R_i = 2.6$: (a) inner cylinder; and (b) outer cylinder.

a very small region near the top of the outer cylinder. The reason for this anomaly can be explained as follows. The buoyant plume rising above the inner cylinder is hotter for the lower radius ratio case, the fluid experiences a greater drop in temperature when it impinges on the outer cylinder. Hence, the temperature gradients at the outer cylinder are greater for the lower radius ratio case. However, the geometry factor (which is found to be more dominant in the lower radius ratio case) causes a slight decrease in the Nusselt number in a small region near the top of the outer cylinder. For $R = 2.6$, 3.5 and 6, the Nusselt number is found to decrease continuously with an increase in radius ratio. The temperature gradients at the outer cylinder decrease continuously with an increase in the radius ratio. This seems to be the more

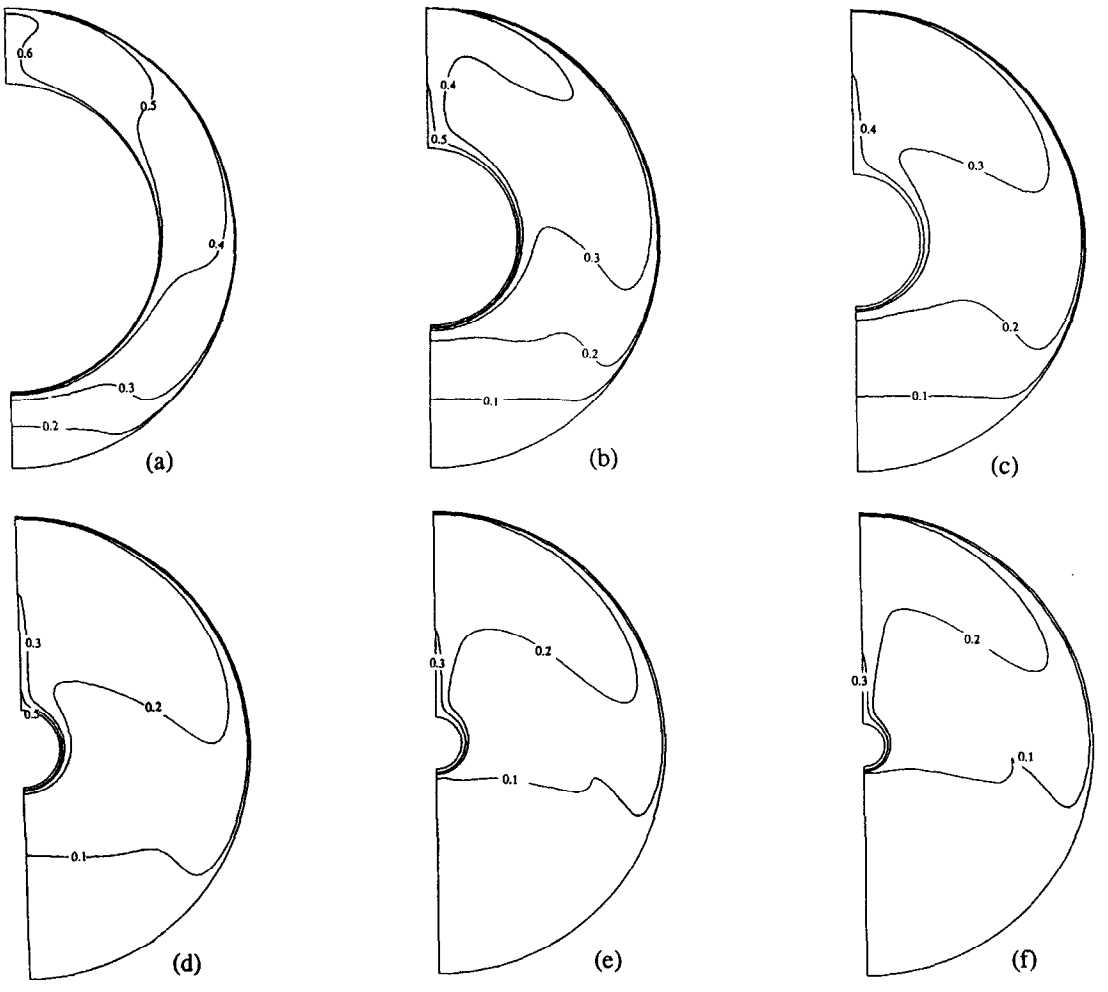

FIG. 12. Temperature distribution at different radius ratios—$Ra = 10^8$ and $Pr = 0.7$: (a) $R_o/R_i = 1.5$; (b) $R_o/R_i = 2.6$; (c) $R_o/R_i = 3.5$; (d) $R_o/R_i = 6$; (e) $R_o/R_i = 9$; and (f) $R_o/R_i = 11$.

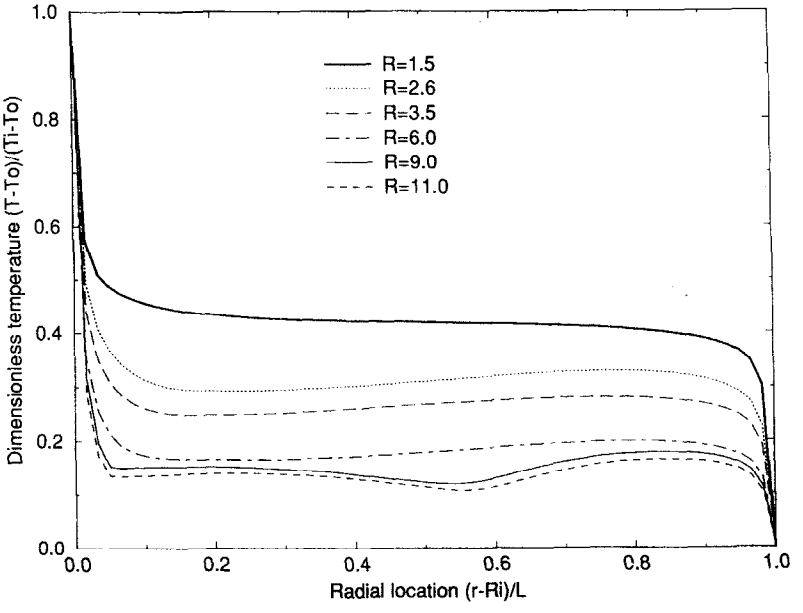

FIG. 13. Temperature distribution in the horizontal plane of the cavity at different radius ratios—$Ra = 10^8$ and $Pr = 0.7$.

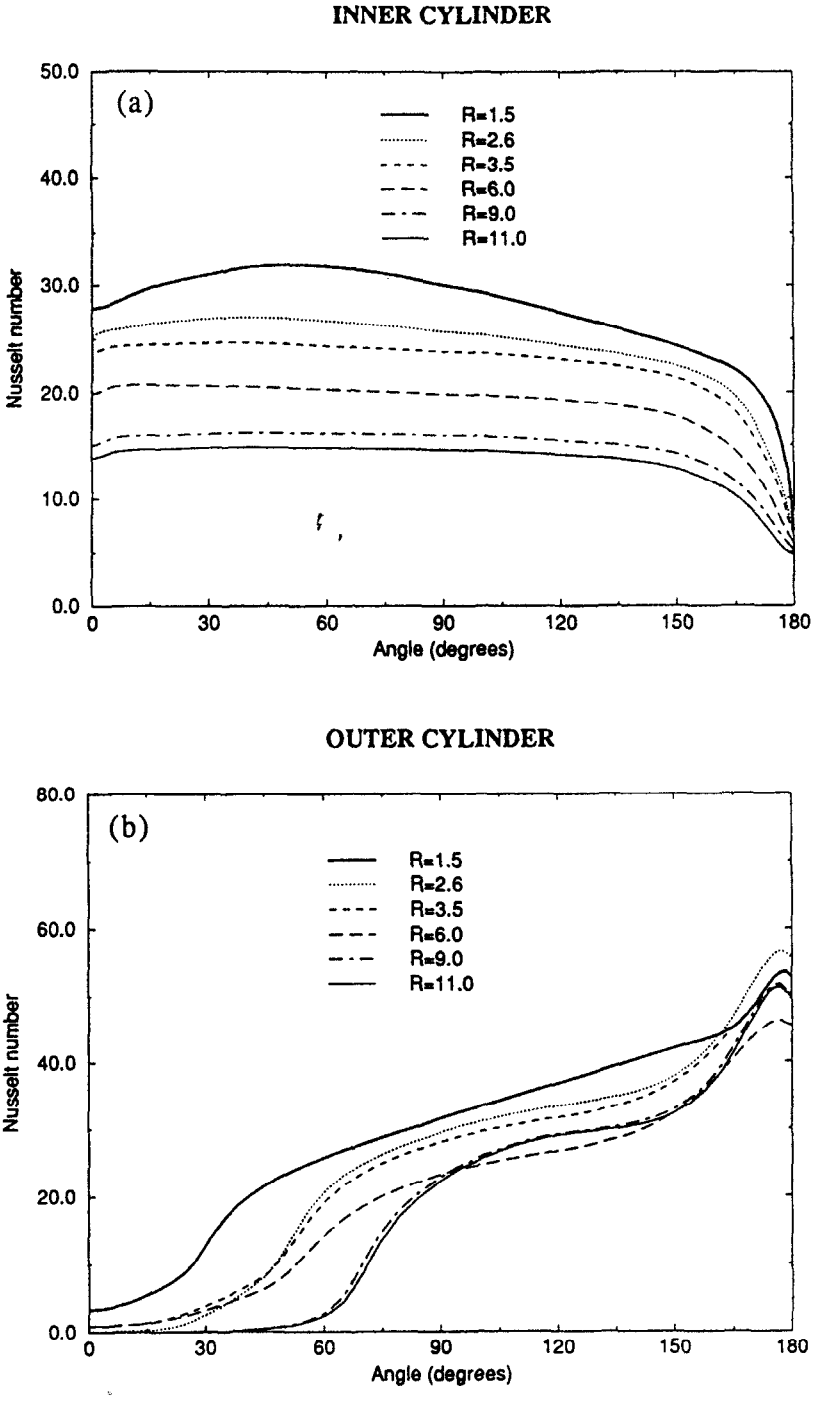

FIG. 14. Nusselt number distribution as a function of radius ratio—$Ra = 10^8$ and $Pr = 0.7$: (a) inner cylinder; and (b) outer cylinder.

influential factor than the geometry factor, causing a decrease in the Nusselt number as the radius ratio increases.

For $R = 9$ and $R = 11$, there is virtually no heat transfer over the lower 45° of the annulus. Since the cylinder dimensions are very small, the energy supplied in the fluid at the inner cylinder is not sufficient to maintain the boundary layer along the entire circumference of the outer cylinder. Hence, the fluid in the lower region is almost stagnant and there is no heat transfer by convection. Beyond 45°, however, heat transfer rapidly increases due to the presence of the thin thermal boundary layer along the outer cylinder. Beyond the horizontal plane, the Nusselt numbers for these cases are higher than for $R = 6$, thus indicating that the geometry factor has a greater influence than the temperature gradient for the cases with $R = 9$ and $R = 11$.

Three-dimensional results

As mentioned before, very few three-dimensional analyses of the turbulent natural convection flow in horizontal annuli have been made in the past. Moreover, none of the three-dimensional solutions to this problem (Fukuda *et al.* [21, 22], Morita *et al.* [23]) have presented the effects of the axial end wall in inducing the three-dimensional behavior within the cavity. Understanding the variation of the Nusselt number over the surfaces of the inner and outer cylinders is very vital from a heat transfer point of view. These issues have not been addressed in previous works. The details of the three-dimensional analysis covered in the present work are somewhat limited due to the tremendous computational effort involved. However, the validity and accuracy of the three-dimensional analysis is amply demonstrated by: (i) the excellent agreement with the corresponding two-dimensional model; and (ii) good agreement with the experimental results.

The wall-function approach used with the two-dimensional study is extended to the three-dimensional model. For the three-dimensional simulations, symmetry about the mid-axial plane was assumed. This was necessary to provide sufficient resolution of the flow and temperature fields without prohibitively expensive computations. The mid-axial symmetry condition was verified by obtaining preliminary computational results for the entire length of the annulus. The mesh was made finer near the walls where steeper gradients were expected to occur and relatively coarse in the core region of the cavity. Eight-noded brick elements with trilinear interpolation and a variable mesh density were used in the entire computational domain.

The first geometry considered for the three-dimensional analysis has a radius ratio of 2.6 (Kuehn and Goldstein [17]). A length to gap-width ratio of 3 was considered for the analysis in order to verify the existence of a core region where the flow is essentially two-dimensional. The calculations were carried out on a mesh containing 33 points in the radial direction, 33 points in the angular direction and 17 points in the axial direction. It is expected that the flow and temperature fields in the axial end-wall region will have a strong three-dimensional behavior because of the viscous shearing effect of the end wall. To study this effect, the temperature distribution within the cavity is presented in Fig. 15. A comparison of isotherms in this core region ($z = L_a/2$; Fig. 15a) against the temperature distribution obtained using the two-dimensional model shows excellent agreement, thus

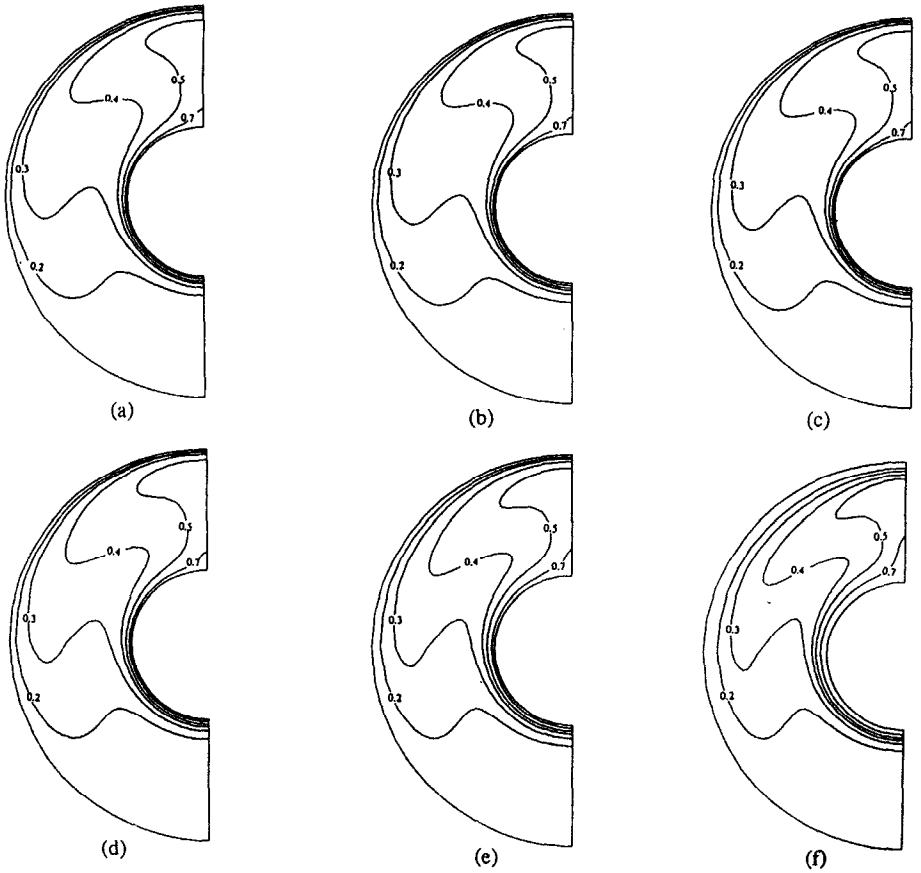

FIG. 15. Temperature distribution at different axial locations—$R_o/R_i = 2.6$, $Ta = 10^6$ and $Pr = 0.7$: (a) $z = L_a/2$ (mid-axial symmetry plane); (b) $z = L_a/3$; (c) $z = L_a/6$; (d) $z = L_a/12$; (e) $z = L_a/24$; and (f) $z = 0$ (axial end wall).

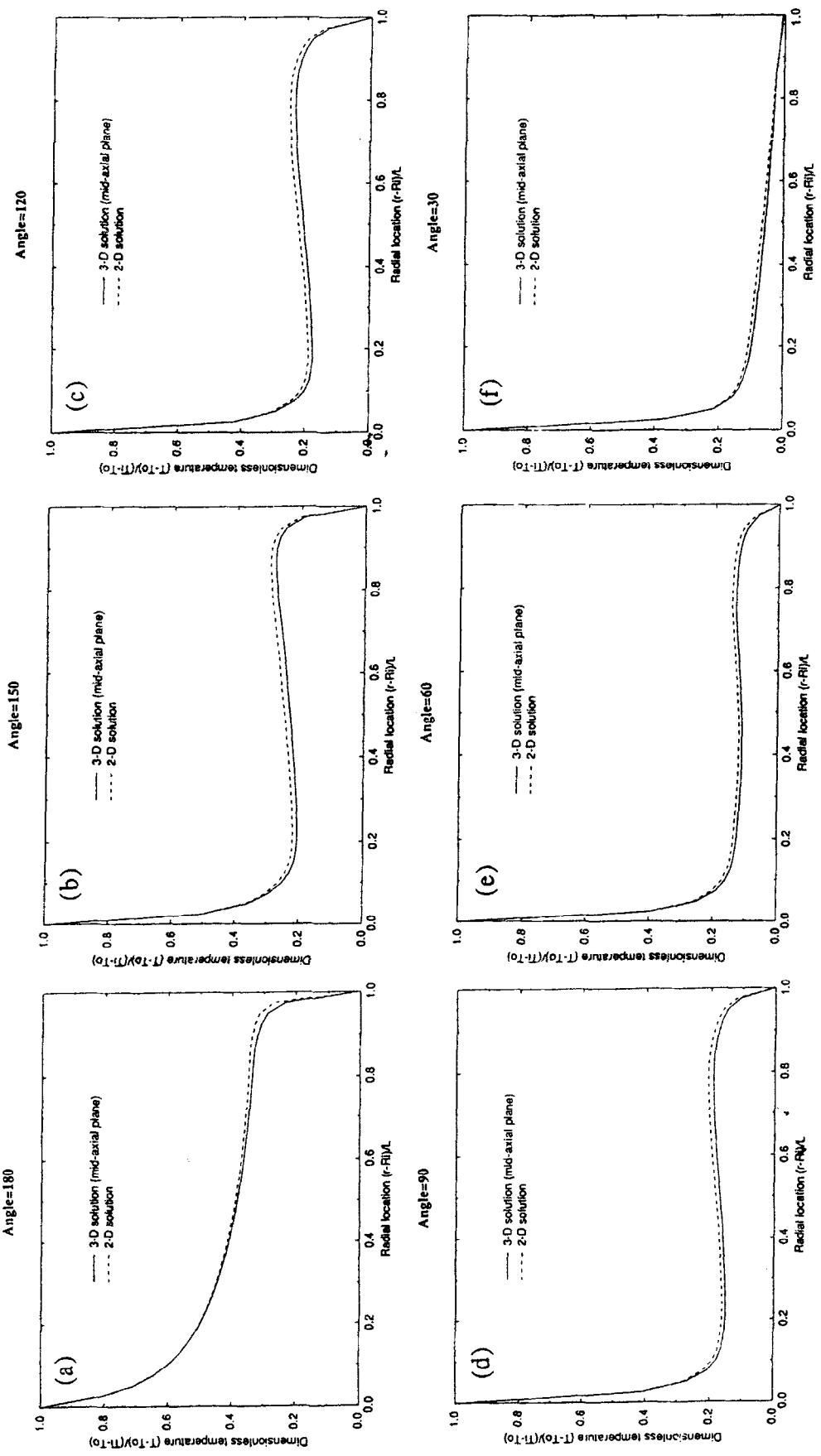

Fig. 16. Comparison of temperature distribution in the core region of the three-dimensional model against the two-dimensional model—$Ra = 1.22 \times 10^7$, $Pr = 0.688$, $R_o/R_i = 4.85$: (a) $\phi = 180^\circ$; (b) $\phi = 150^\circ$; (c) $\phi = 120^\circ$; (d) $\phi = 90^\circ$; (e) $\phi = 60^\circ$; and (f) $\phi = 30^\circ$.

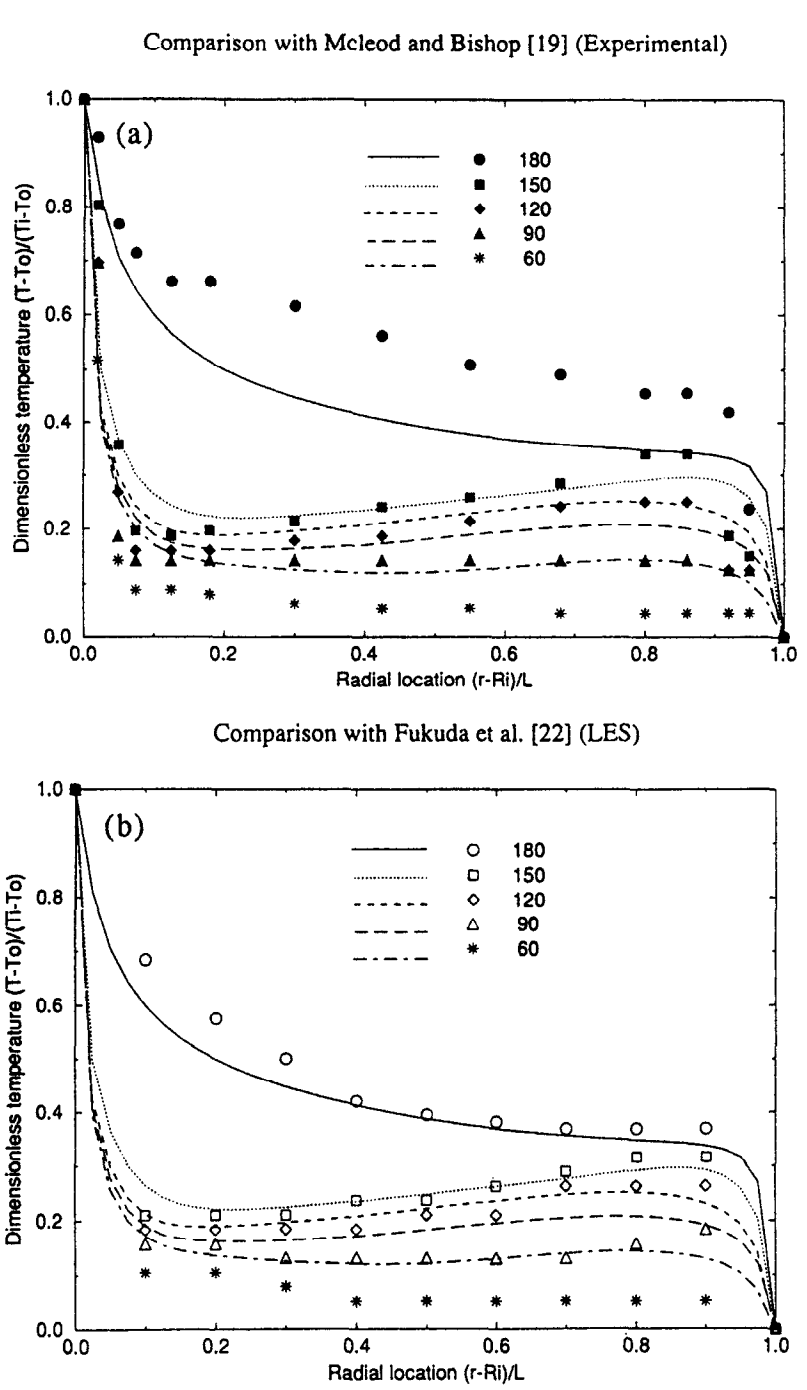

FIG. 17. Comparison of results from the three-dimensional model against previous experimental and numerical results $Ra = 1.22 \times 10^7$, $Pr = 0.688$ and $R_o/R_i = 4.85$.

further confirming that the assumption of two-dimensionality in the core region is valid. However, at $z = L_a/12$, $L_a/24$ and 0 (end wall), the temperature distribution changes remarkably. The reduction in the strength of the convective flow causes the temperature gradients around the inner and outer cylinders to decrease.

An examination of the flow field within the cavity showed the existence of a spirally rotating flow which is characteristic of annular cavity natural convection flows as shown in the work of Vafai and Ettefagh [7]. The heat transfer rates in the mid-section of the cavity followed the same trend as demonstrated by the two-dimensional results presented earlier. The Nusselt numbers in the core region approach the turbulent two-dimensional results. As was anticipated from the temperature distribution, the core region in which the axial variations were negligible was found to persist for approximately 3/4 times the length of the annulus. The Nusselt number decreases drastically in the region

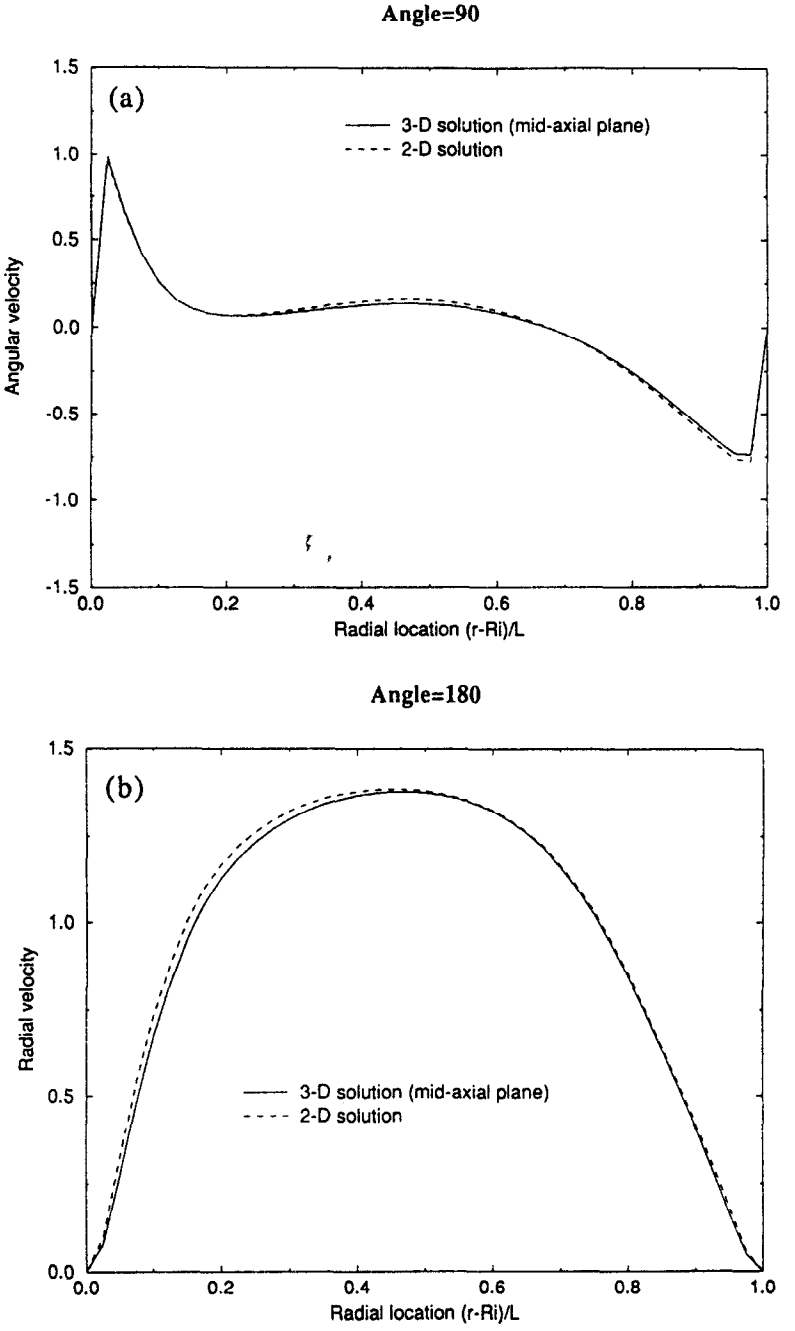

FIG. 18. Comparison of the velocity profiles in the mid-axial symmetry plane ($z = 0$) of the three-dimensional model against the two-dimensional model—$Ra = 1.22 \times 10^7$, $Pr = 0.688$, $R_o/R_i = 4.85$: (a) angular velocity at $\phi = 90^\circ$; and (b) radial velocity at $\phi = 180^\circ$.

very close to the end walls because of the decrease of the strength of the convective flow in the near-wall region.

Another set of calculations was performed for an annulus with a radius ratio of 4.85. McLeod and Bishop [19] have presented detailed experimental results for this geometry. Results were obtained for a Rayleigh number of 1.22×10^7 and a Prandtl number of 0.688. A sufficient amount of experimentation was done to determine the length of the annulus which would provide a core region in which the results can be approximated by using a two-dimensional model. It was concluded that an annulus length to gap-width ratio of at least 7.5 was necessary for this purpose. Since we also wanted to establish the collapse of the three-dimensional solution to the corresponding two-dimensional results in the mid-axial plane of the annulus, it was necessary to use the same number of grid

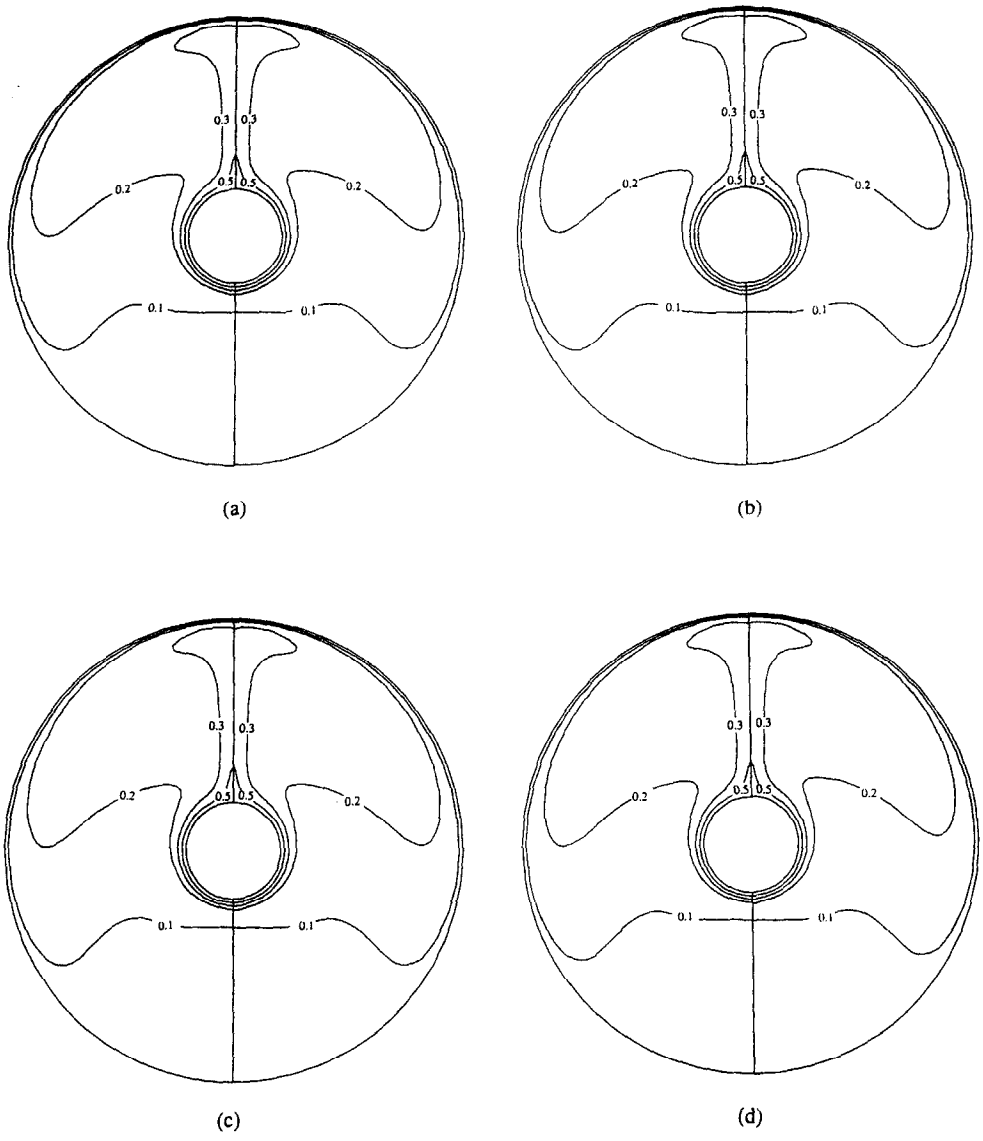

FIG. 19. Comparison of isotherms in different axial planes of the cavity (left-hand side) against the mid-axial symmetry plane (right-hand side)—$Ra = 1.22 \times 10^7$, $Pr = 0.688$, $R_o/R_i = 4.85$: (a) $z = 7L_a/16$, $L_a/2$; (b) $z = 3L_a/8$, $L_a/2$; (c) $z = 5L_a/16$, $L_a/2$; and (d) $z = L_a/4$, $L_a/2$.

points in the radial and angular directions for both models. A 41×41 grid was employed for the two-dimensional study while a $41 \times 41 \times 31$ grid was used for the three-dimensional study. As mentioned before, the 41×41 grid with a mesh grading ratio of 2 was adequate to give flow field and temperature results that were independent of the mesh size. However, to give grid independent Nusselt number results, a finer mesh was required. Hence, for the present three-dimensional runs, we used a mesh grading ratio of 4, i.e. the mesh size near the wall was 1/4 times the mesh size in the interior region of the domain, to capture the steep gradients near the solid boundaries, giving accurate Nusselt number results. With this method of grading, it was observed that all results showed negligible variation with further reduction in mesh size.

Figure 16 shows a comparison of the temperature distribution at the mid-axial symmetry plane ($z = 0$) obtained from the three-dimensional model against the results from the two-dimensional solution. A comparison of the temperature distributions at six different angular locations showed excellent agreement. The maximum difference between the temperatures predicted by the two models is less than 3%. Both models succeeded in capturing the steep gradients near the walls of the cavity. The temperature distribution was also compared against the experimental results of McLeod and Bishop [19] and the LES simulations of Fukuda *et al.* [22] and were found to be in good agreement (Fig. 17). As mentioned previously, the discrepancies between the experimental and numerical results is because of the fact that constant fluid properties have been used in the present analysis. Due to the

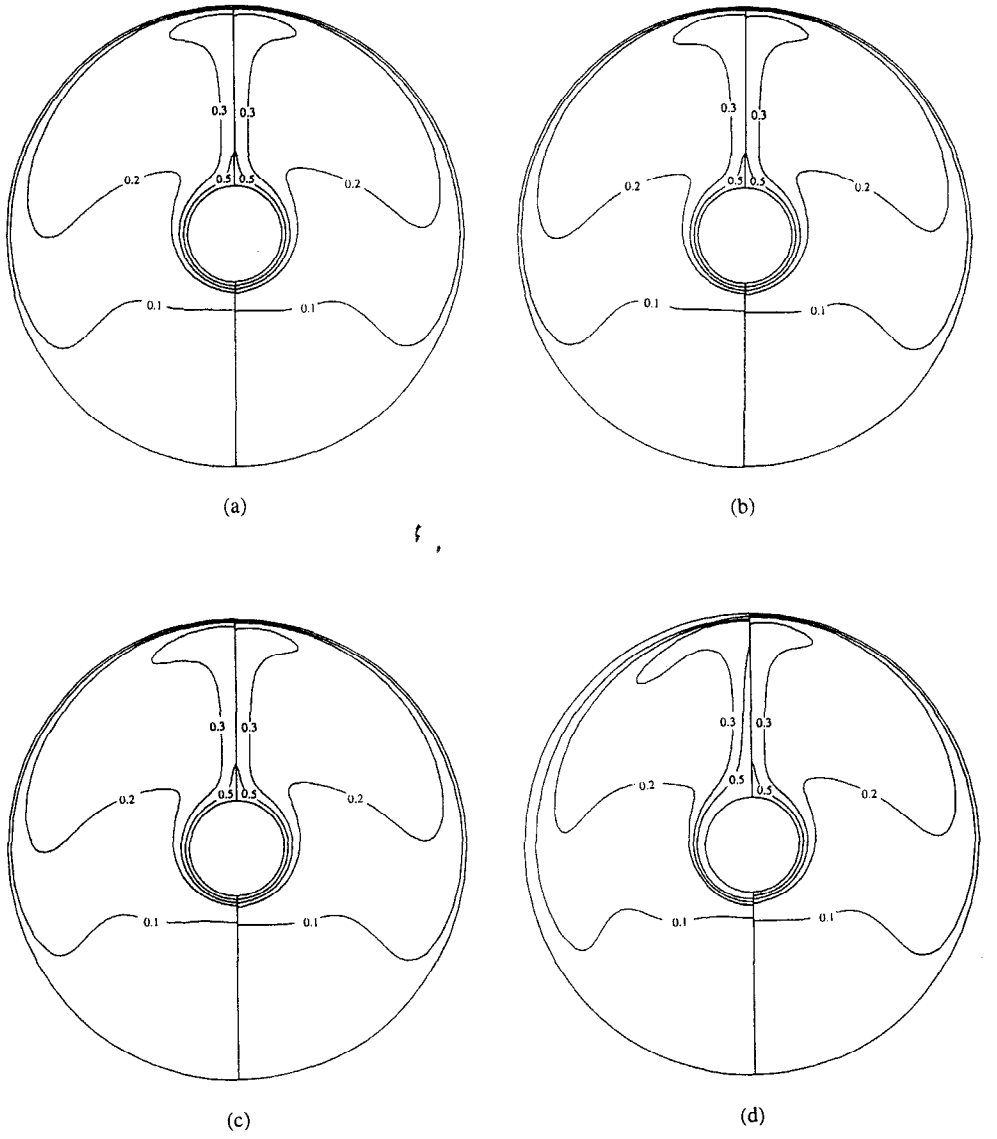

FIG. 20. Comparison of isotherms in different axial planes of the cavity (left-hand side) against the mid-axial symmetry plane (right-hand side)—$Ra = 1.22 \times 10^7$, $Pr = 0.688$, $R_o/R_i = 4.85$: (a) $z = 3L_a/16$, $L_a/2$; (b) $z = L_a/8$, $L_a/2$; (c) $z = L_a/16$, $L_a/2$; and (d) $z = 0$, $L_a/2$.

high temperature differences involved in the present case, this assumption could lead to some inaccuracies. Another reason for the discrepancy is due to the temperature measurements. Since probes of some kind are introduced within the flow for performing the temperature measurement, this induces errors due to the perturbation of the natural convection flow field. To establish the two-dimensionality of the flow field in the core region of the annulus, the velocity profiles obtained from the two models were compared. This was done by comparing the angular velocity profiles in the horizontal plane of the annulus (90°) and the radial velocity profiles in the top vertical plane (180°) from the two models. As can be seen from Fig. 18, the flow fields obtained from the two models are in excellent agreement with each other.

The existence of the core region within the annulus was verified by comparing the isotherms at different axial locations of the cavity with the isotherms in the mid-axial symmetry plane ($z = 0$) of the cavity. Figures 19 and 20 show this comparison. In each case, the right-hand side represents the isotherms in the mid-axial plane whereas the left-hand side represents the isotherms in selected axial planes of the cavity one-sixth of the annulus length apart. From $z = L_a/16$ to $z = 3L_a/8$, the temperature distribution in the cavity is identical to the temperature distribution in the mid-axial symmetry plane of the annulus. This is apparent from the temperature distribution shown in Figs. 19 and 20a and b. Hence, in this region of the annulus, the temperature field is essentially invariant in the axial direction and can therefore be approximated by the use of a two-dimensional model. Beyond $z = 3L_a/8$, the temperature distribution devi-

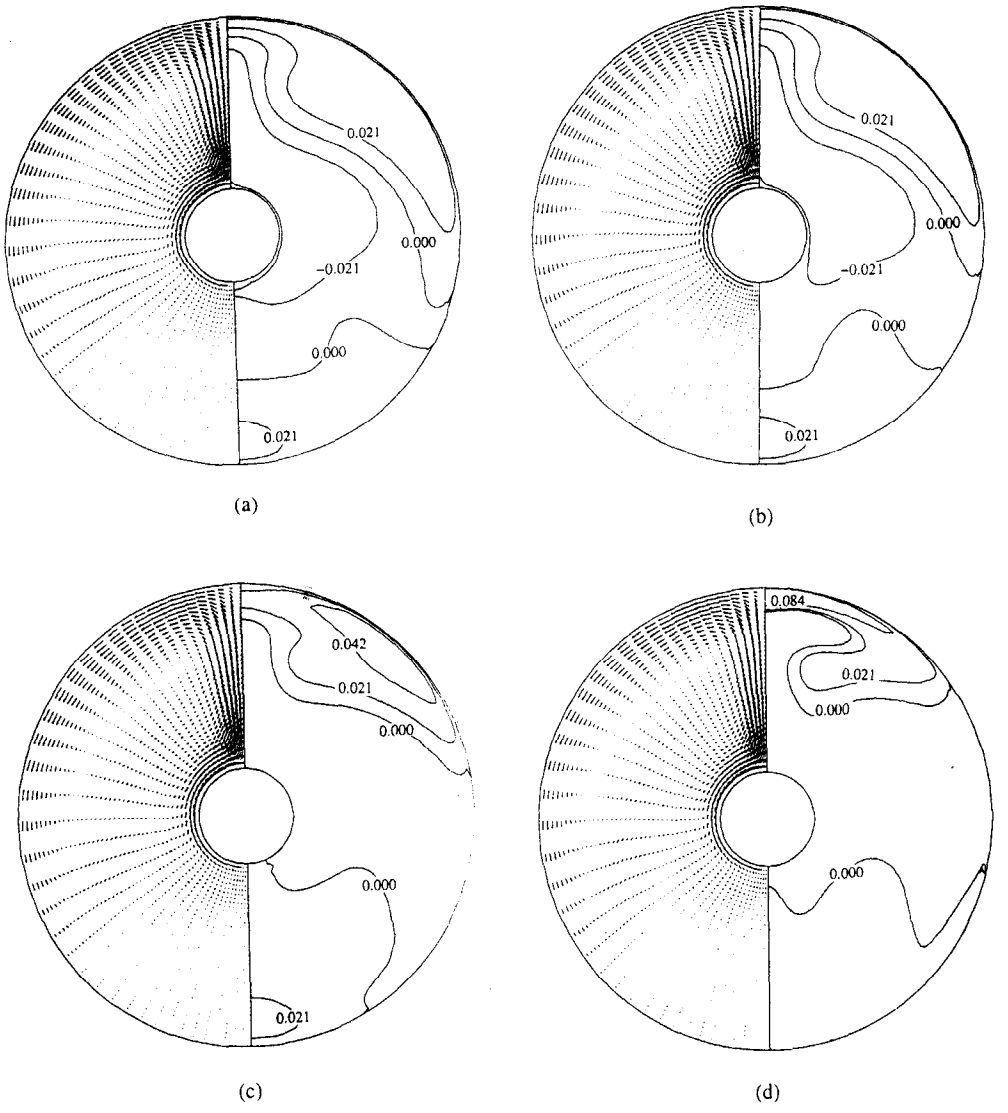

FIG. 21. Flow field in different axial planes of the annulus $Ra = 1.22 \times 10^7$, $Pr = 0.688$, $R_o/R_i = 4.85$: (a) $z = L_a/8$; (b) $z = 3L_a/32$; (c) $z = L_a/16$; and (d) $z = L_a/32$.

ates from the core region temperature distribution as shown in Fig. 20c and d. The gradients around the inner and outer cylinders reduce drastically because of the reduction in the strength of the convective flow in the radial planes of the annulus.

In Fig. 21, the three-dimensional structure of the flow field is presented as a combination of plots showing the velocity vector field in the radial plane (on the left-hand side) and contours of axial velocity (on the right-hand side). Only four locations very close to the solid end wall were chosen for presenting these results, since the axial velocity values beyond this location are very small. The velocity vector field follows the crescent shaped recirculation pattern in each radial plane of the annulus. Flow occurs in the positive axial direction, i.e. toward the axial end walls in the top and bottom region of the annulus and close to the outer cylinder. This is balanced by an axial flow in the opposite direction in the remaining portion of the radial plane. The axial velocities are found to be very low in the core region and increase continuously toward the solid wall, thus showing the existence of strong three-dimensionality effects in the near-wall region. The maximum values of the velocity vector in the four locations shown in the figure are, respectively, 1.3955, 1.3948, 1.3934 and 1.3466, thus showing that the viscous shearing effect of the axial end-wall causes a reduction in the velocity.

A comparison of the inner and outer cylinder Nusselt numbers in the mid-axial plane of the annulus and the corresponding two-dimensional model is shown in Fig. 22. The Nusselt numbers in the mid-axial plane of the annulus agreed very well with the results from the two-dimensional analysis (a maximum difference of 2% was observed). The average Nusselt number (equivalent conductivity) was compared with the value obtained from the correlation of McLeod and Bishop [19]. The present study gave an average Nus-

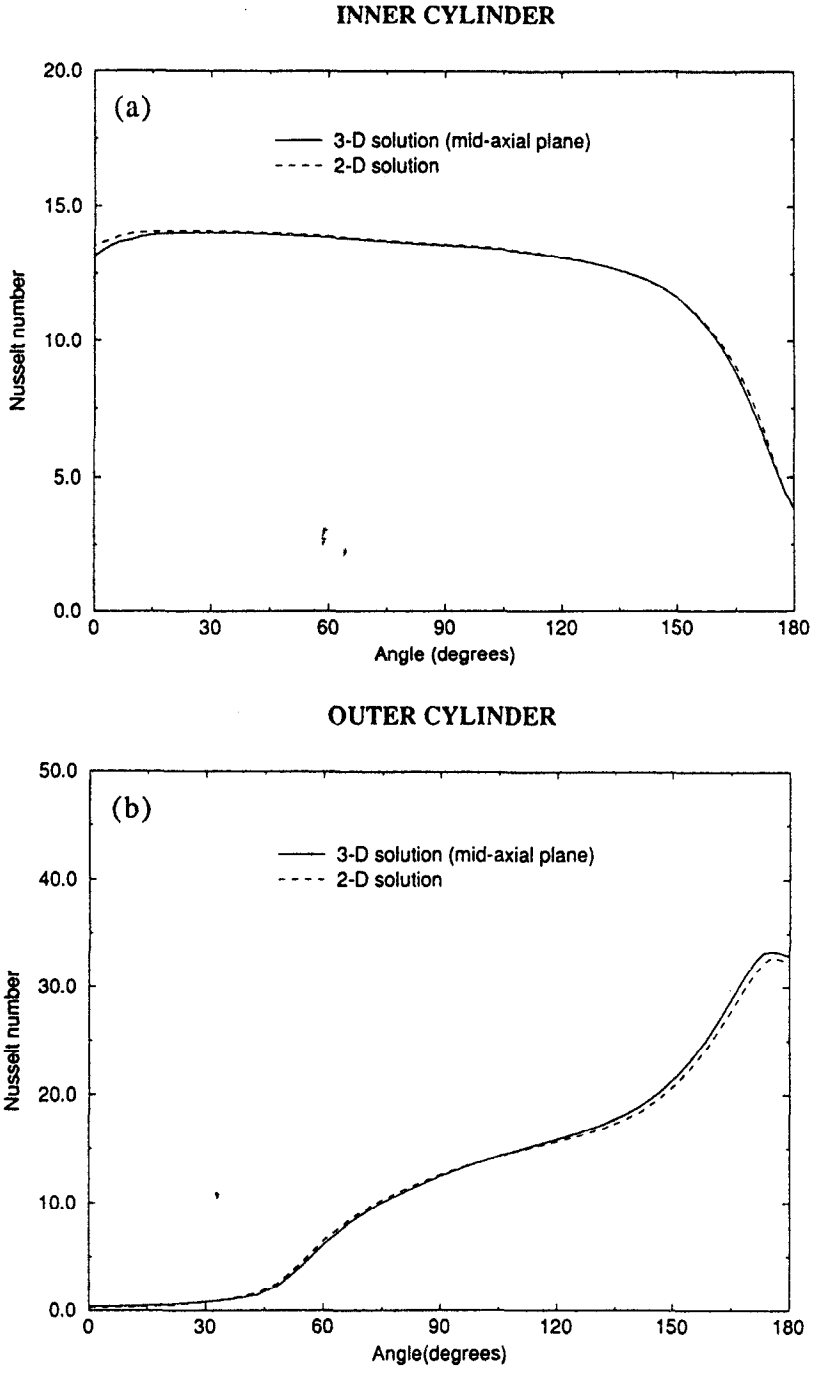

FIG. 22. Comparison of local Nusselt numbers in the mid-axial symmetry plane ($z = 0$) of the three-dimensional model against the two-dimensional model. $Ra = 1.22 \times 10^7$, $Pr = 0.688$, $R_o/R_i = 4.85$: (a) inner cylinder; and (b) outer cylinder.

selt number value of 13.04 while the value predicted by McLeod and Bishop [19] was 12.84, which differed by only 1.53%. The local Nusselt number distribution over the inner and outer cylinder surfaces is shown in Fig. 23. As expected, the Nusselt number distribution over the inner and outer cylinders remains unchanged in the core region of the annulus, thus demonstrating the validity of the two-dimensional assumption over a significant portion of the core region. Near the end-walls of the annulus, however, the Nusselt number distribution changes significantly. As reduction in the strength of the convective flow causes the heat transfer rates over the inner and outer cylinder surfaces to decrease considerably. Very close to the axial end walls, the heat transfer from both the inner and outer cylinders is virtually negligible. For the outer cylinder, however, a local peak in the Nusselt number distribution was observed near the top of the annulus

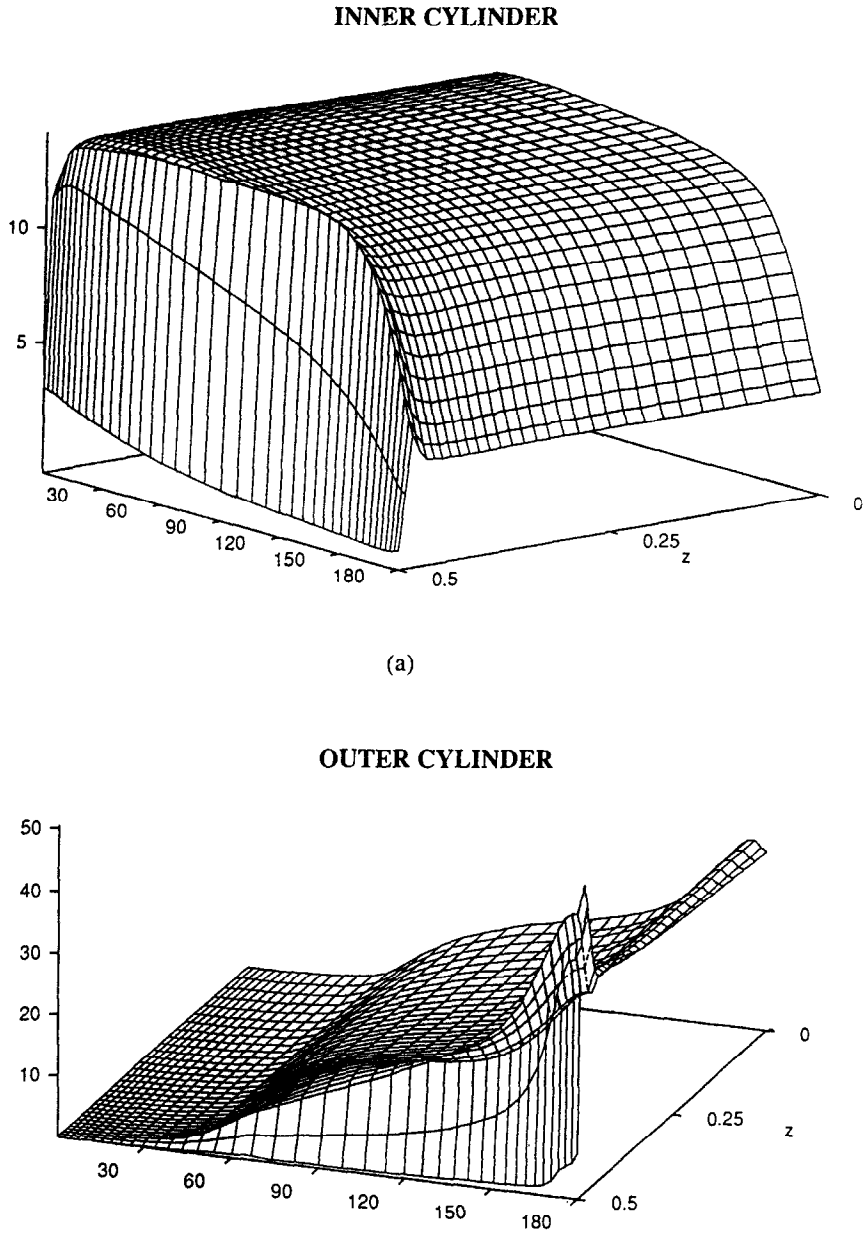

FIG. 23. Nusselt number distribution over the inner and outer cylinders—$Ra = 1.22 \times 10^7$, $Pr = 0.688$, $R_o/R_i = 4.85$: (a) inner cylinder; and (b) outer cylinder.

and very close to the axial end wall. The reason for this high value of the heat transfer rate is the presence of high axial velocities in this region.

CONCLUSIONS

A comprehensive investigation of turbulent natural convection between concentric, horizontal cylinders has been successfully carried out. Both two- and three-dimensional models have been used to obtain results in the present study. An in-depth study of the thermophysical and geometric characteristics has been carrried out using the two-dimensional model. The contours of turbulent kinetic energy and turbulent viscosity indicate highest turbulence intensities in the upper portion of the annulus and also in the region near the inner cylinder where boundary-layer separation occurs. The heat transfer results obtained in the present study are summarized in Table 1. These results show the effect of Rayleigh number, Prandtl

Table 1. Mean cavity Nusselt numbers for the various cases studied

Parameter								
Ra	*Pr*	*Gr*	$R_o/R_i = 1.5$	$R_o/R_i = 2.6$	$R_o/R_i = 3.5$	$R_o/R_i = 6$	$R_o/R_i = 9$	$R_o/R_i = 11$
10^8	0.01	10^{10}		11.9527				
10^6	0.7			9.1541				
10^7	0.7			15.484				
10^8	0.7		26.761	22.214	21.733	18.074	14.2789	12.9664
10^8	7			28.425				
10^8	100	10^6		32.31				
10^8	1000	10^5		28.4236				
10^8	5000	2×10^4		29.0531				

number and radius ratio on the heat transfer coefficients associated with the natural convection flow. Heat transfer rates are found to be substantially higher than those in the laminar regime. The results show a decrease in heat transfer rates from the inner and outer cylinders with an increase in radius ratio for the same Rayleigh number based on the gap-width. The effect of Prandtl number was also investigated. The turbulent viscosity was found to decrease for fluids with higher Prandtl numbers, thus indicating lower levels of turbulence. The transition to turbulence gets delayed for high Prandtl number fluids. The three-dimensional simulations were carried out to study the effect of the end walls on the natural convection process. It was observed that the Nusselt number undergoes a drastic decrease at the end walls. The decrease in Nusselt number at the end walls is substantial in the turbulent regime because of the more prominent damping effect of the end walls at high Rayleigh numbers.

This work provides informative data for turbulent natural convection in annular geometries of two and three dimensions, different aspect ratios and containing fluids with a wide range of properties. The two-dimensional approach has been extended to a three-dimensional model to provide more realistic insight into the structure of the flow and temperature fields. To the best of the authors' knowledge, these are the first documented results on detailed three-dimensional flow and temperature characteristics as well as detailed investigation of various thermophysical and geometric characteristics of two-dimensional more complicated geometries.

Acknowledgements— The support of the DOE under grant DE-FG02-93ER61612 for part of this work is acknowledged and appreciated, and the authors would like to also acknowledge and thank Mr Mark Dyko for his helpful comments on our work.

REFERENCES

1. T. H. Kuehn and R. J. Goldstein, An experimental and theoretical study of natural convection in the annulus between horizontal concenric cylinders. *J Fluid Mech.* **74,** 695–719 (1976).
2. Y. T. Tsui and B. Tremblay, On transient natural convection heat transfer in the annulus between concentric horizontal cylinders with isothermal surfaces, *Int. J. Heat Mass Transfer* **27,** 103–111 (1984).
3. R. Kumar, Study of natural convection in horizontal annuli, *Int. J. Heat Mass Transfer* **31,** 1137–1148 (1988).
4. A. Castrejon and D. B. Spalding, An experimental and theoretical study of transient free-convection flow between horizontal concentric cylinders, *Int. J. Heat Mass Transfer* **31,** 273–284 (1988).
5. Y. Takata, K. Iwashige, K. Fukuda and S. Hasegawa, Three-dimensional natural convection in an inclined cylindrical annulus, *Int. J. Heat Mass Transfer* **27,** 747–754 (1984).
6. T. Fusegi and B. Farouk, A three-dimensional study of natural convection in an inclined cylindrical annulus, *Proceedings of the Eighth International Heat Transfer Conference*, **4,** 1575–1580 (1986).
7. K. Vafai and J. Ettefagh, An investigation of transient three-dimensional bouyancy-driven flow and heat transfer in a closed horizontal annulus, *Int. J. Heat Mass Transfer* **34,** 2555–2570 (1991).
8. J. A. C. Humphrey and W. M. To, Numerical simulation of buoyant turbulent flow—I. Free convection along a heated vertical flat plate, *Int. J. Heat Mass Transfer* **29,** 573–592 (1986).
9. N. C. Markatos, M. R. Malin and G. Cox, Mathematical modeling of buoyancy-induced smoke flow in enclosures, *Int. J. Heat Mass Transfer* **25,** 63–75 (1982).
10. B. E. Launder and D. B. Spalding, The numerical computation of turbulent flows, *Computer Meth. Appl. Mech. Engng* **3,** 269–289 (1974).
11. N. C. Markatos and K. A. Pericleous, Laminar and turbulent natural convection in an enclosed cavity, *Int. J. Heat Mass Transfer* **27,** 755–772 (1984).
12. H. Ozoe, A. Mouri, M. Ohmuro, S. W. Churchill and N. Lior, Numerical calculations of laminar and turbulent and natural convection in water in rectangular channels heated and cooled isothermally on the opposing vertical walls, *Int. J. Heat Mass Transfer* **28,** 125–138 (1985).
13. J. A. C. Humphrey and W. M. To, Numerical simulation of buoyant turbulent flow—II. Free and mixed convection in a heated cavity, *Int. J. Heat Mass Transfer* **29,** 593–610 (1986).
14. W. P. Jones and B. E. Launder, The prediction of laminarization with a two-equation model of turbulence, *Int. J. Heat Mass Transfer* **15,** 301–314 (1972).
15. R. A. W. M. Henkes, F. F. Van Der Vlugt and C. J. Hoogendoorn, Natural convection flow in a square cavity calculated with low-Reynolds-number turbulence models, *Int. J. Heat Mass Transfer* **34,** 377–388 (1991).
16. K.-Y. Chien, Predictions of channel and boundary layer flows with a low-Reynolds-number two-equation model of turbulence, AIAA-80-0134 (1980).
17. T. H. Kuehn and R. J. Goldstein, An experimental study of natural convection heat transfer in concentric and eccentric horizontal cylindrical annuli, *ASME J. Heat Transfer* **100,** 635–640 (1978).

18. E. H. Bishop, Heat transfer by natural convection of helium between horizontal isothermal concentric cylinders at cryogenic temperature, *ASME J. Heat Transfer* **110,** 109–115 (1988).
19. A. E. McLeod and E. H. Bishop, Turbulent natural convection of gases in horizontal cylindrical annuli at cryogenic temperatures, *Int. J. Heat Mass Transfer* **32,** 1967–1978 (1989).
20. B. Farouk and S. I. Guceri, Laminar and turbulent natural convection in the annulus between horizontal concentric cylinders, *ASME J. Heat Transfer* **104,** 631–636 (1982).
21. K. Fukuda, Y. Miki and S. Hasegawa, Analytical and experimental study on turbulent natural convection in a horizontal annulus, *Int. J. Heat Mass Transfer* **33,** 629–639 (1990).
22. K. Fukuda, Y. Miki, N. Taniguchi, K. Morita and S. Hasegawa, Direct simulation and large eddy simulation of turbulent natural convection in horizontal annulus, *Memoirs of Faculty of Engineering—Kyushu University* **51,** 355–369 (1991).
23. K. Morita, Y. Nakamura, N. Taniguchi, K. Fukuda and S. Hasegawa, Unsteady three-dimensional behavior of natural convection in horizontal annulus—validity of direct numerical simulation of turbulent natural convection, *J. Atomic Energy Soc. Japan* **32,** 719–727 (1990).
24. M. P. Fraikin, J. J. Portier and C. J. Fraikin, Application of a k–ε turbulence model to an enclosed buoyancy driven recirculating flow, 19th ASME–AIChE Nat. Heat Transfer Conference Paper, 80-HT-68 (1980).
25. M. Ciofalo and M. W. Collins, k ε predictions of heat transfer in turbulent recirculating flows using an improved wall treatment, *Numer. Heat Transfer B* **15,** 21–47 (1989).
26. V. Haroutunian and M. S. Engelman, On modeling wall-bound turbulent flows using specialized near-wall finite elements and the standard k–ε turbulence model, *Adv. Numer. Simulation Turbulent Flows: ASME-FED* **117,** 97–105 (1991).
27. H. Reichardt, Die Grundlagen des turbulenten Warmeuberganges, *Arch. Gesamte Waermetech.* **2,** 129–142 (1951).
28. C. L. V. Jayatilleke, The influence of Prandtl number and surface roughness on the resistance of the laminar sublayer to momentum and heat transfer, *Prog. Heat Mass Transfer* **1,** 193–329 (1969).
29. *FIDAP Theoretical Manual.* Fluid Dynamics International, Evanston, IL, U.S.A.
30. K. Vafai and C. P. Desai, Comparative analysis of the finite-element and finite-difference methods for simulation of buoyancy-induced flow and heat transfer in closed and open-ended annular cavities, *Numer. Heat Transfer A* **23,** 35–59 (1993).
31. F. Wolff, C. Beckermann and R. Viskanta, Natural convection of liquid metals in vertical cavities, *Exper. Thermal Fluid Sci.* **1,** 83–91 (1988).
32. A. Bejan, *Convection Heat Transfer.* John Wiley (1984).
33. R. E. Powe, C. T. Carley and E. H. Bishop, Free convective flow patterns in cylindrical annuli, *ASME J. Heat Transfer* **91,** 310–314 (1969).